

1 **Tidal intrusion fronts, surface convergence, and mixing in an estuary with  
2 complex topography**

3 Tong Bo<sup>a b c</sup>, David K. Ralston<sup>a</sup>, Adrian Mikhail P. Garcia<sup>a b d</sup>, W. Rockwell Geyer<sup>a</sup>

4 <sup>a</sup> *Applied Ocean Physics and Engineering Department, Woods Hole Oceanographic Institution,  
5 Woods Hole, MA 02543, United States*

6 <sup>b</sup> *MIT-WHOI Joint Program in Oceanography/Applied Ocean Science and Engineering,  
7 Cambridge, MA 02139, United States*

8 <sup>c</sup> *Department of Atmospheric and Oceanic Sciences, University of California Los Angeles, Los  
9 Angeles, CA 90095, United States*

10 <sup>d</sup> *Exponent, Inc., Bellevue, WA 98007, United States*

11 *Corresponding author:* Tong Bo, tbo@whoi.edu

<sup>12</sup> ABSTRACT: Observations from a tidal estuary show that tidal intrusion fronts occur regularly  
<sup>13</sup> during flood tides near topographic features including constrictions and bends. A realistic model  
<sup>14</sup> is used to study the generation of these fronts and their influence on stratification and mixing in the  
<sup>15</sup> estuary. At the constriction, flow separation occurs on both sides of the jet flow downstream of the  
<sup>16</sup> narrow opening, leading to sharp lateral salinity gradients and baroclinic secondary circulation.  
<sup>17</sup> A tidal intrusion front, with a V-shaped convergence zone on the surface, is generated by the  
<sup>18</sup> interaction between secondary circulation and the jet flow. Stratification is created at the front  
<sup>19</sup> due to the straining of lateral salinity gradients by secondary circulation. Though stratification  
<sup>20</sup> is expected to suppress turbulence, strong turbulent mixing is found near the surface front. The  
<sup>21</sup> intense mixing is attributed to enhanced vertical shear due to both frontal baroclinicity and the  
<sup>22</sup> twisting of lateral shear by secondary circulation. In the bend, flow separation occurs along  
<sup>23</sup> the inner bank, resulting in lateral salinity gradients, secondary circulation, frontogenesis, and  
<sup>24</sup> enhanced mixing near the front. In contrast to the V-shaped front at the constriction, an oblique  
<sup>25</sup> linear surface convergence front occurs in the bend, which resembles a one-sided tidal intrusion  
<sup>26</sup> front. Moreover, in addition to baroclinicity, channel curvature also affects secondary circulation,  
<sup>27</sup> frontogenesis, and mixing in the bend. Overall in the estuary, the near-surface mixing associated  
<sup>28</sup> with tidal intrusion fronts during flood tides is similar in magnitude to bottom boundary layer  
<sup>29</sup> mixing that occurs primarily during ebbs.

30 **1. Introduction**

31 Surface fronts are ubiquitous in estuaries (e.g., Simpson and Turrell 1986; Largier 1992;  
32 O'Donnell 1993). As regions where two distinct water masses interact and generate sharp density  
33 gradients (Largier 1993), estuarine surface fronts usually have strong horizontal convergence due  
34 to baroclinicity from the frontal density gradient (Valle-Levinson et al. 2000; Giddings et al. 2012;  
35 Collignon and Stacey 2012). The convergence means these surface features are typically identifi-  
36 ciable by accumulated foam and debris, in addition to sharp color discontinuities that are often  
37 visible (Brown et al. 1991; Largier 1992). Correspondingly, fronts have important implications for  
38 transport and aggregation of pollutants, phytoplankton, and larvae (Tyler et al. 1982; Brown et al.  
39 1991; Wang et al. 2022).

40 Examples of surface fronts in estuaries include tidal intrusion fronts (Simpson and Nunes 1981),  
41 axial convergence fronts (Nunes and Simpson 1985), and plume fronts (Garvine 1974). These  
42 categories are not mutually independent – e.g., tidal intrusion fronts, which appear as denser  
43 water intrudes into a basin of buoyant water, are dynamically similar to plume fronts that form  
44 when buoyant water discharges into a region with denser water (O'Donnell 1993). Both tidal  
45 intrusion fronts and axial convergence fronts result from the differential advection of longitudinal  
46 density gradients by tidal currents (Simpson and Turrell 1986), and axial convergence fronts have  
47 been observed to originate at the apex of tidal intrusion fronts (Largier 1992). Moreover, axial  
48 convergence fronts can produce buoyancy-driven flow structures that propagate away from the  
49 generation region as plume fronts (O'Donnell 1993).

50 This research focuses on tidal intrusion fronts that form as seawater is advected into estuaries by  
51 flood tide currents. Tidal intrusion fronts typically exhibit a V-shaped configuration, with horizontal  
52 re-circulation zones on both sides of the front and intense surface convergence along the centerline  
53 (Simpson and Nunes 1981; Largier 1992). Nevertheless, the mechanisms of frontogenesis and  
54 mixing investigated here apply to other surface fronts with different morphologies but similar  
55 dynamics, as will be discussed later.

56 Topographic complexity, e.g., channel constrictions, shallow shoals, confluences, headlands, and  
57 meanders, are often important sites for estuarine frontogenesis (e.g., Largier 1992; Giddings et al.  
58 2012; Geyer and Ralston 2015). Complex topographic features can generate 3-d flow structures  
59 that interact with the salinity field, and fronts are created as secondary circulation sharpens salinity

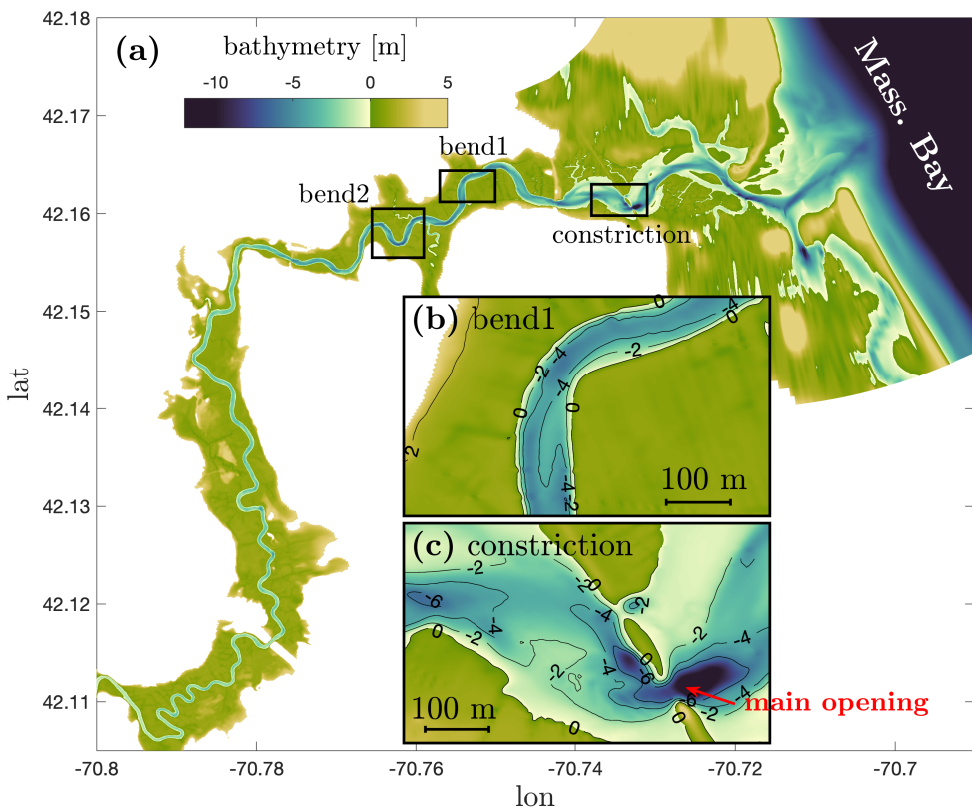
gradients through normal or shear straining (McWilliams 2021). Constrictions and channel-shoal bathymetry can lead to strong lateral shear in tidal flows and create lateral salinity gradients through differential advection (Nunes and Simpson 1985; Lacy et al. 2003; Collignon and Stacey 2012; Li et al. 2014). The associated lateral baroclinic forcing drives secondary circulation in the channel cross-section, resulting in lateral convergence near the surface, increasing lateral salinity gradients, and contributing to frontogenesis. In addition to differential advection, lateral salinity fronts may result from lateral trapping by side channels or mudflats (Valle-Levinson et al. 2000; Giddings et al. 2012; Garcia et al. 2021), with baroclinic dynamics and secondary circulation similar to differential advection. In channel bends, curvature can drive secondary circulation through the centrifugal acceleration in the lateral momentum balance (Thomson 1877; Kalkwijk and Booij 1986; Geyer 1993). The development of secondary circulation, as well as its interaction with the salinity field and influence on frontogenesis, thus depends on both centrifugal acceleration and baroclinic forcing in sinuous estuaries (Lacy and Monismith 2001; Nidzieko et al. 2009; Becherer et al. 2015; Kranenburg et al. 2019).

In addition to its influence on frontogenesis, secondary circulation associated with topographic complexity plays crucial roles in affecting stratification, vertical mixing, and horizontal dispersion. For example, secondary circulation and lateral straining of salinity gradients can increase or decrease stratification (Lacy et al. 2003; Giddings et al. 2012; Scully and Geyer 2012; Becherer et al. 2015; Bo and Ralston 2022). In a shallow estuary in the Salish Sea, Giddings et al. (2012) observed that a surface front and the associated secondary circulation led to enhanced stratification in late flood tide, thus suppressing vertical turbulent mixing. In contrast, Collignon and Stacey (2013) reported that secondary circulation was responsible for turbulence generation in late ebb tides at the channel-shoal interface in South San Francisco Bay. Similarly, in the James River, Huguenard et al. (2015) found that near-surface turbulence and mixing was related to secondary circulation during ebb tides. Secondary circulation associated with topographic complexity, e.g., channel-shoal systems and meanders, can also affect the subtidal structure of salinity and longitudinal velocity fields, thereby impacting the landward salt flux (e.g., Lerczak and Geyer 2004; Ralston and Stacey 2005; Becherer et al. 2015; Geyer et al. 2020)

In this research, we conduct a numerical modeling study of the North River estuary (MA, USA), an intermittently stratified, shallow tidal channel with complex topography (Kranenburg et al.

2019; Bo et al. 2021; Garcia et al. 2021). Surface fronts have been regularly observed during flood tides at multiple locations along the estuary, and fronts are particularly associated with topographic features like channel constrictions and bends. We investigate in detail the frontal structures and associated secondary circulation at two representative locations, a constriction and a bend. The influences of fronts and secondary circulation on stratification and turbulent mixing in the estuary are also examined. In section 2, we introduce the study site, model setup, observations, and the theoretical framework for studying secondary circulation, stratification, and mixing. Section 3 presents the results and analysis, and we discuss their implications in section 4. Section 5 is a conclusion.

## 99 2. Methods



100 FIG. 1. (a): North River estuary model bathymetry. The constriction is located at around 2 km into the estuary.  
 101 Bend1 is at around 4 km into the estuary, and this bend is selected for detailed model analysis. Bend2 is at around  
 102 5.5 km into the estuary, where drone imagery was obtained. (b): Bathymetry of the bend region (bend1). (c):  
 103 Bathymetry of the constriction region.

<sup>104</sup> *a. Study site*

<sup>105</sup> The North River estuary (MA, USA) is a sinuous tidal channel that connects to Massachusetts  
<sup>106</sup> Bay (Fig. 1 **(a)**). The typical channel depth is around 5 m and width is 50–100 m. The tides in the  
<sup>107</sup> estuary are dominantly semi-diurnal, with a tidal range between 2 m and 4 m (Kranenburg et al.  
<sup>108</sup> 2019; Bo et al. 2021). The maximum tidal velocity in the estuary varies between 0.5 m/s and 1 m/s  
<sup>109</sup> with the neap-spring cycle. The freshwater discharge is usually less than 10 m<sup>3</sup>/s, corresponding  
<sup>110</sup> to a mean velocity of < 0.05 m/s, but can be up to 30 m<sup>3</sup>/s due to rainfall events. The salinity  
<sup>111</sup> intrusion distance typically varies from around 8 km to 14 km (Garcia et al. 2021).

<sup>112</sup> Two examples of characteristic topographic features are a channel constriction at 2 km into the  
<sup>113</sup> estuary (Fig. 1 **(c)**) and a channel bend at 4 km (bend1 in Fig. 1 **(b)**). In the constriction region,  
<sup>114</sup> constructed embankments from an abandoned railroad impose lateral topographic constraints on  
<sup>115</sup> the channel. The main opening is on the south side with a width of 40 m and depth of 10 m  
<sup>116</sup> (Fig. 1 **(c)**). A smaller, secondary opening is on the north side with a width of less than 10 m and  
<sup>117</sup> depth less than 1 m. Landward of the constriction, the channel expands to 100–200 m wide, and  
<sup>118</sup> a shallow shoal in the southern part of the channel has a depth of ~ 2 m. The channel curvature is  
<sup>119</sup> mild near the constriction, with a radius of curvature of around 300 m. In this study, we focus on  
<sup>120</sup> the main opening that conveys most of the tidal exchange.

<sup>121</sup> In the bend at around 4 km, the channel undergoes a nearly 90-degree turn (bend1 in Fig. 1 **(b)**)  
<sup>122</sup> with a radius of curvature of around 100 m. The channel width is 60–80 m and is relatively  
<sup>123</sup> uniform through the bend, and the depth is around 5 m. Other bends in the mid- and lower estuary  
<sup>124</sup> similarly have widths of 50–100 m and radii of curvature of 50–300 m. This corresponds to  
<sup>125</sup> curvature ratios (bend sharpness) of around 1–5, which is in the typical range for natural river and  
<sup>126</sup> tidal meanders (Leopold and Wolman 1960; Marani et al. 2002). The bend at 4 km is selected as a  
<sup>127</sup> representative example, but similar surface fronts and frontal dynamics occur in many other bends  
<sup>128</sup> in the North River estuary.

<sup>129</sup> *b. Numerical simulations*

<sup>130</sup> The Regional Ocean Modeling System (ROMS) (Shchepetkin and McWilliams 2005; Haidvogel  
<sup>131</sup> et al. 2008; Warner et al. 2008, 2010) is used to simulate the North River estuary (Fig. 1 **(a)**). An  
<sup>132</sup> orthogonal curvilinear grid is built that extends from Massachusetts Bay to around 18 km into the

estuary. The finest horizontal resolution is 3 m in the channel (around 10–30 grid cells across the channel) and grid spacing increases offshore and in the marsh away from the channel. A terrain-following coordinate with 16 uniformly distributed layers is used in the vertical direction. The  $k-\epsilon$  closure of the generic length-scale (GLS) turbulence closure scheme is used for the vertical mixing (Umlauf and Burchard 2003; Warner et al. 2005). The bottom roughness  $z_0$  is a uniform of 0.005 m in the domain, except that  $z_0$  is locally increased to 0.2 m in a section with large rocks on the bed located around 7 km from the mouth to better represent the decrease in tidal amplitude in that region. A third-order upwind advection scheme is used for horizontal advection. The horizontal mixing coefficient is 0.01 m<sup>2</sup>/s, and it is small enough to have no appreciable influence on the resulting velocity structure. The wetting and drying algorithm (Warner et al. 2013) is employed to simulate tidal inundation and drainage over the marsh platform and shallow shoals within the channel. The critical depth for shutting off volumetric flux from a grid cell is set to 0.02 m.

The simulations cover a one-month period from early October to early November in 2021. Tidal fluctuations on the ocean boundaries were extracted from the ADCIRC database (Luettich et al. 1992). Subtidal fluctuations were obtained from the low-pass filtered (Butterworth filter, with a cut off period of 33 hours) water surface elevation record from the National Oceanic and Atmospheric Administration (NOAA) station at Boston (#8443970). River discharge was input as a freshwater source on the western boundary based on data from the U.S. Geological Survey (USGS) gauge at Hanover (#01105730) multiplied by 2.3 to account for freshwater inputs below the gauge. Wind forcing was not included in the model.

The model setup is essentially the same as that described by Bo et al. (2023) to study the hydrodynamic drag and salt intrusion in the North River. The model was evaluated in Bo et al. (2023) by comparing it with the measured tidal water levels, velocities, and salinity from long-term moorings and shipboard surveys in 2017. In this research, we focus on simulations of a one-month period in 2021, and the model results are compared with observations in 2021 (described in the following section) for a skill assessment (Murphy 1988). The skill scores are higher than 0.95 for water level, in the range of 0.9 to 0.95 for velocity, and around 0.8 for salinity (Fig. 2).

160 *c. Field observations*

161 Field measurements were made in the North River estuary from September to November 2021.  
162 Four long-term moorings were deployed at around 0 km, 2 km (near the constriction), 5 km,  
163 and 8 km into the estuary. At each mooring, pressure and salinity time series were measured by  
164 conductivity-temperature-depth (CTD) sensors mounted near the surface and the bed. Velocity  
165 profile data were collected at each of the three seaward mooring sites by an upward-looking  
166 Aquadopp profiler mounted on the bed. The long-term measurements of water level, salinity, and  
167 velocity were used for model assessment. In addition, aerial drone imagery of surface fronts was  
168 obtained at multiple topographic features, including the constriction and several bends, by a DJI  
169 Phantom 4 drone. The drone imagery was used to characterize the structures of surface fronts.

170 *d. Theoretical framework*

171 To develop the theoretical framework for analyzing tidal intrusion fronts, stratification, and  
172 mixing, we first introduce the momentum and vorticity equations for secondary circulation with  
173 curvature (sections 2 d 1 and 2 d 2). Next, an analysis of the tendency of the gradient Richardson  
174 number is used to assess the effects of secondary circulation on water column stability (section 2 d 3).  
175 Finally, we present the salinity variance budget to quantify the stratification, straining, and mixing  
176 associated with tidal intrusion fronts (section 2 d 4).

177 1) MOMENTUM EQUATIONS

178 The streamwise and lateral momentum equations for flow with curvature are

$$\frac{Du}{Dt} = -g \frac{\partial \eta}{\partial x} - \beta g \int_z^\eta \frac{\partial s}{\partial x} dz + \text{sgn}(R) \frac{uv}{R} + \frac{\partial}{\partial z} K_v \frac{\partial u}{\partial z}, \quad (1a)$$

$$\frac{Dv}{Dt} = -g \frac{\partial \eta}{\partial y} - \beta g \int_z^\eta \frac{\partial s}{\partial y} dz - \text{sgn}(R) \frac{u^2}{R} + \frac{\partial}{\partial z} K_v \frac{\partial v}{\partial z}, \quad (1b)$$

179 where

$$\frac{D}{Dt} = \frac{\partial}{\partial t} + u \frac{\partial}{\partial x} + v \frac{\partial}{\partial y} + w \frac{\partial}{\partial z}. \quad (2)$$

180 The local coordinates generally follow the channel orientation, with  $x$ ,  $y$ ,  $z$  being the streamwise,  
181 lateral, and vertical directions, and  $u$ ,  $v$ ,  $w$  being the corresponding velocity components.  $+x$

182 is generally eastward (ebb direction) in the study area of the North River, and  $+y$  is generally  
 183 northward (90-degree counterclockwise rotation of the ebb direction).  $\eta$  is water level and  $s$  is  
 184 salinity.  $\beta$  is the haline contraction coefficient and  $K_v$  is the vertical eddy viscosity.  $R$  is the radius  
 185 of curvature;  $\text{sgn}(R) > 0$  when the  $+y$  direction is toward the center of the bend, and vice versa.  
 186 Note that here  $\frac{D}{Dt}$  is not the material derivative because this study employs curvilinear coordinates  
 187 instead of Cartesian coordinates. Non-inertial terms (curvature forcing terms) arise in curvilinear  
 188 coordinates, i.e., the third terms on the right side of (1a) and (1b), and the non-inertial term in (1b)  
 189 is usually referred to as the centrifugal forcing. We use the expression  $\frac{D}{Dt}$  and put the non-inertial  
 190 terms on the right side for the convenience of the following analysis. Coriolis has been neglected  
 191 as it is usually not important in small estuaries like the North River.

192 To study the terms responsible for secondary circulation, we subtract the depth-averaged (1b)  
 193 from (1b) (e.g., Geyer 1993; Chant and Wilson 1997; Nidzieko et al. 2009) and write

$$\underbrace{\frac{\partial v}{\partial t}}_{\text{unsteady}} + \underbrace{\left( u \frac{\partial v}{\partial x} - \bar{u} \overline{\frac{\partial v}{\partial x}} \right)}_{\text{advection}} = \underbrace{-\beta g \left( \int_z^\eta \frac{\partial s}{\partial y} dz - \int_z^\eta \frac{\partial s}{\partial y} dz \right)}_{\text{BCPG}} - \underbrace{\text{sgn}(R) \frac{u^2 - \bar{u}^2}{R}}_{\text{CFA}} + \underbrace{\left( \frac{\partial}{\partial z} K_v \frac{\partial v}{\partial z} + \frac{\tau_{b,y}}{\rho H} \right)}_{\text{friction}}, \quad (3)$$

194 with an overbar representing the depth average, and  $\bar{v} = 0$  by definition. The lateral and vertical  
 195 advection terms have been neglected.  $\tau_{b,y} = K_v (\partial v / \partial z)|_{bed}$  is the lateral component of the bed  
 196 shear stress, and surface stress is zero in the model.  $H$  is water depth and  $\rho$  is density. The first term  
 197 on the left side is the unsteady term (time rate of change). The second term represents streamwise  
 198 advection, i.e., the downstream adjustment of secondary circulation (e.g., Nidzieko et al. 2009).  
 199 The first term on the right side is the baroclinic pressure gradient force (BCPG), and the second  
 200 term is the centrifugal acceleration (CFA), and the third term is friction.

## 201 2) VORTICITY EQUATIONS

202 In addition to the momentum balance, we use the streamwise component of vorticity  $\omega_x$  to  
 203 quantify secondary circulation following Becherer et al. (2015). The vertical shear of lateral  
 204 velocity usually dominates over the lateral shear of vertical velocity in determining  $\omega_x$ , since  
 205  $v \gg w$  and  $\Delta y \gg \Delta z$ . In a similar way, we can identify the lateral component of vorticity  $\omega_y$  as the  
 206 vertical shear of streamwise velocity. Therefore, we write

$$\omega_x = \frac{\partial w}{\partial y} - \frac{\partial v}{\partial z} \approx -\frac{\partial v}{\partial z}; \quad (4a)$$

$$\omega_y = \frac{\partial u}{\partial z} - \frac{\partial w}{\partial x} \approx \frac{\partial u}{\partial z}. \quad (4b)$$

207 Taking the vertical derivative of (1), substituting in (4), and rearranging

$$\frac{D\omega_x}{Dt} = -\beta g \frac{\partial s}{\partial y} + \frac{\partial v}{\partial x} \omega_y - \left( \frac{\partial v}{\partial y} + \frac{\partial w}{\partial z} \right) \omega_x + \text{sgn}(R) \frac{2}{R} u \omega_y + \mathcal{R}_{\omega_x}; \quad (5a)$$

$$\frac{D\omega_y}{Dt} = \beta g \frac{\partial s}{\partial x} + \frac{\partial u}{\partial y} \omega_x - \left( \frac{\partial u}{\partial x} + \frac{\partial w}{\partial z} \right) \omega_y - \text{sgn}(R) \frac{1}{R} u \omega_x + \mathcal{R}_{\omega_y}. \quad (5b)$$

208 The equation for  $\omega_x$  (5a) is essentially a representation of the lateral momentum balance (3). While  
209 the momentum balance straightforwardly shows the terms responsible for lateral flows, the vorticity  
210 approach can provide a more consistent framework for understanding the generation and interaction  
211 of vorticity components (Becherer et al. 2015), and vorticity directly links to the vertical shear that  
212 affects mixing processes. Note that in (5), we have written out the baroclinicity, vorticity twisting,  
213 vorticity stretching (associated with divergence/convergence), and curvature terms, and we collect  
214 the remaining terms in  $\mathcal{R}_{\omega_x}$  and  $\mathcal{R}_{\omega_y}$ , e.g., turbulent viscosity (friction).

215 3) WATER COLUMN STABILITY

216 We apply a gradient Richardson number analysis in a similar manner as Collignon and Stacey  
217 (2013) to investigate the effects of secondary circulation on stability and mixing. The gradient  
218 Richardson number  $Ri_g$  is defined as

$$Ri_g = \frac{N^2}{S^2} = \frac{-\beta g \frac{\partial s}{\partial z}}{\left( \frac{\partial u}{\partial z} \right)^2 + \left( \frac{\partial v}{\partial z} \right)^2}, \quad (6)$$

219 where  $S$  is the total vertical shear, and  $N$  is the buoyancy frequency.

$$N = \left( -\frac{g}{\rho_0} \frac{\partial \rho}{\partial z} \right)^{\frac{1}{2}} = \left( -\beta g \frac{\partial s}{\partial z} \right)^{\frac{1}{2}}, \quad (7)$$

as temperature is uniform in the model and the density only depends on salinity.  $Ri_g$  compares the stabilizing effect of stratification to the destabilizing effect of vertical shear (Miles 1961; Collignon and Stacey 2013). A critical value  $Ri_{g,cr} \approx 0.25$  is used for determining the growth of instability in the water column (Miles 1961; Howard 1961). Shear can overcome stratification when  $Ri_g < Ri_{g,cr}$ , which allows for the growth of turbulence and mixing; stratification damps instabilities when  $Ri_g > Ri_{g,cr}$  such that turbulence and mixing are inhibited.

The tendency equation for  $Ri_g$  is assessed to identify the influences of secondary circulation on water column stability and mixing by taking the derivative of (6):

$$\frac{D Ri_g}{Dt} = \frac{1}{S^2} \left[ -\beta g \frac{D}{Dt} \left( \frac{\partial s}{\partial z} \right) - 2Ri_g \frac{\partial u}{\partial z} \frac{D}{Dt} \left( \frac{\partial u}{\partial z} \right) - 2Ri_g \frac{\partial v}{\partial z} \frac{D}{Dt} \left( \frac{\partial v}{\partial z} \right) \right]. \quad (8)$$

The first term on the right side corresponds to the tendency of the vertical salinity gradient  $\partial s / \partial z$ . The other two terms correspond to the tendency of vertical shear, which depends on the vorticity dynamics in (5). The evolution of  $\partial s / \partial z$  can be written as

$$\frac{D}{Dt} \left( \frac{\partial s}{\partial z} \right) = -\frac{\partial u}{\partial z} \frac{\partial s}{\partial x} - \frac{\partial v}{\partial z} \frac{\partial s}{\partial y} - \frac{\partial w}{\partial z} \frac{\partial s}{\partial z} + \mathcal{R}_S, \quad (9)$$

which is found by taking the vertical derivative of salinity transport equation. The first two terms on the right side represent the straining of horizontal salinity gradients by the vertically sheared horizontal flow. The third term represents the stretching/compressing of vertical salinity gradients associated with vertical divergence/convergence. Note that this stretching/compressing term is the normal straining of vertical salinity gradients, and we name it in this way to avoid confusion with the shear straining described by the first two terms. Vertical mixing is collected in the remainder term  $\mathcal{R}_S$ .

238 Substituting (4), (5), and (9) into (8), we can therefore quantitatively characterize the competing  
 239 effects of vertical shear and salinity gradients on  $Ri_g$ :

$$\frac{DRi_g}{Dt} = \frac{1}{S^2} \left\{ \underbrace{\beta g \left( -\omega_x \frac{\partial s}{\partial y} + \omega_y \frac{\partial s}{\partial x} \right)}_{\text{salinity strain.}} + \underbrace{2Ri_g \beta g \left( \omega_x \frac{\partial s}{\partial y} - \omega_y \frac{\partial s}{\partial x} \right)}_{\text{shear, baroc.}} - \underbrace{2Ri_g \omega_x \omega_y \left( \frac{\partial u}{\partial y} + \frac{\partial v}{\partial x} \right)}_{\text{shear, twist.}} \right. \\ \left. + \underbrace{\beta g \frac{\partial w}{\partial z} \frac{\partial s}{\partial z}}_{\text{salinity stretch.}} + \underbrace{2Ri_g \left[ \left( \frac{\partial v}{\partial y} + \frac{\partial w}{\partial z} \right) \omega_x^2 + \left( \frac{\partial u}{\partial x} + \frac{\partial w}{\partial z} \right) \omega_y^2 \right]}_{\text{shear, stretch.}} - \underbrace{2Ri_g \omega_x \omega_y \text{sgn}(R) \frac{u}{R} + \mathcal{R}_{R_I}}_{\text{shear, curv.}} \right\} \quad (10)$$

240 The first term on the right side represents the salinity straining processes that affect  $Ri_g$  by creating  
 241 stratification. Horizontal salinity gradients can not only be converted to stratification by straining,  
 242 but also have a tendency to drive gravity currents and enhance the shear through baroclinicity, and  
 243 this shear generation process is represented by the second term. The third term on the right side  
 244 results from the interplay of vorticity components (the twisting of horizontal shear into vertical  
 245 shear). The fourth term corresponds to the effects of stretching/compressing of vertical salinity  
 246 gradients on  $Ri_g$ . The fifth term represents the influence of divergence/convergence on vertical  
 247 shear. The sixth term represents contributions from channel curvature. The remainder term  $\mathcal{R}_{R_I}$   
 248 involves the effects of  $\mathcal{R}_{\omega_x}$ ,  $\mathcal{R}_{\omega_y}$ , and  $\mathcal{R}_S$  on  $Ri_g$ , e.g., turbulent mixing of salinity and the turbulent  
 249 viscosity (mixing of momentum). The potential influences of these terms on  $Ri_g$  dynamics will  
 250 be discussed later. Through the  $Ri_g$  tendency analysis, we can assess the water column stability  
 251 by incorporating both the salinity straining and the stretching/compressing that affect stratification  
 252 and the different sources of shear that cause turbulence.

253 Note that the first and second terms on the right side of (10) are similar expressions but have  
 254 opposite signs because horizontal salinity gradients have competing influences on  $Ri_g$ . Straining of  
 255 horizontal salinity gradients can create stratification that stabilizes the water column while vertical  
 256 shear due to a gravity current can induce turbulence and reduce stability. The first two terms can  
 257 thus be rewritten as  $(1 - 2Ri_g)$  times the horizontal salinity gradient and vertical shear. These two  
 258 terms alone would lead to a net tendency to decrease  $Ri_g$  to 0.5 for  $Ri_g > 0.5$ , which can explain  
 259 the  $Ri_g$  dynamics for a freely propagating 2-d gravity current with a uniform horizontal density  
 260 gradient (Simpson and Linden 1989).

261 4) VERTICAL SALINITY VARIANCE BUDGET

262 To assess the overall influence of secondary circulation and tidal intrusion fronts on stratification  
 263 we use the vertical salinity variance budget. The depth-integrated vertical salinity variance budget  
 264 (Burchard and Rennau 2008; Li et al. 2018) is

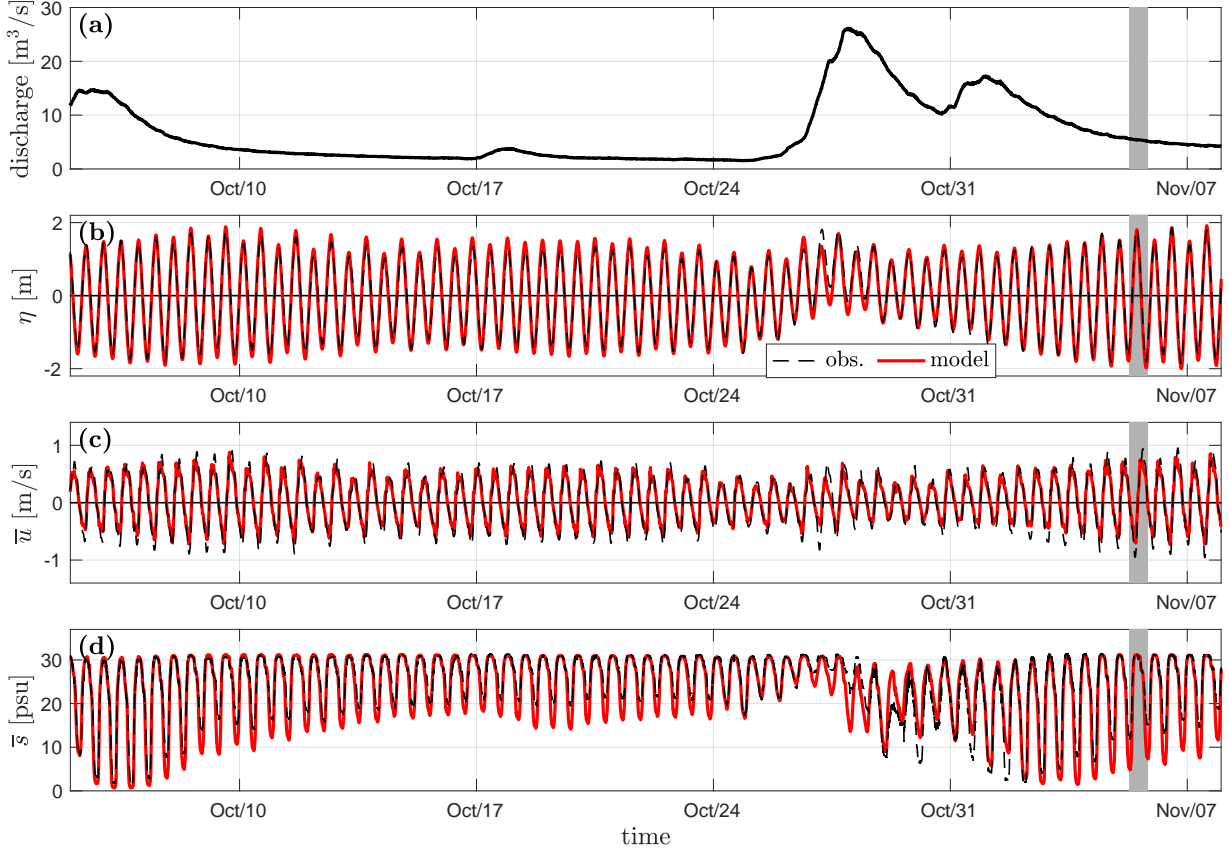
$$\underbrace{\frac{\partial}{\partial t} \int (s'_v)^2 dz}_{\text{unsteady}} - \underbrace{\nabla_h \cdot \int \mathbf{u}(s'_v)^2 dz}_{\text{advection}} - \underbrace{\int 2\mathbf{u}'_v s'_v \cdot \nabla_h \bar{s} dz}_{\text{straining}} - \underbrace{\int 2K_s \left(\frac{\partial s}{\partial z}\right)^2 dz}_{\text{turb. mixing}} - \underbrace{\int \mathcal{M}_{num} dz}_{\text{num. mixing}}. \quad (11)$$

265  $\bar{s}$  is the depth-averaged salinity, and  $s'_v$  is the deviation from the depth average.  $(s'_v)^2$  is the  
 266 vertical salinity variance that corresponds with stratification in the water column.  $\nabla_h$  is the  
 267 horizontal gradient operator.  $\mathbf{u} = (u, v)$  is the horizontal velocity vector, and  $\mathbf{u}'_v$  represents the  
 268 vertical deviations of horizontal velocity.  $K_s$  is the eddy diffusivity for vertical salinity mixing.  
 269 The left-side term represents the temporal change of the vertical salinity variance. The first term  
 270 on the right side represents advection, and the second term represents straining (same as the shear  
 271 straining process in (9) above, but here adapted for the vertical salinity variance). The third term is  
 272 turbulent mixing that irreversibly dissipates the vertical variance. The fourth term is the additional  
 273 numerical mixing  $\mathcal{M}_{num}$  that arises from discretization errors of the tracer advection scheme in  
 274 the model.  $\mathcal{M}_{num}$  is calculated as the difference between the advected square of the tracer and the  
 275 square of advected tracer (e.g., Burchard and Rennau 2008; Ralston et al. 2017; Kalra et al. 2019).

276 3. Results and analysis

277 a. Estuarine conditions

278 During the observation period of October and November 2021, the tidal range in the North River  
 279 estuary was between 2 m and 4 m, with a tidal velocity amplitude of 0.4 – 0.8 m/s (Fig. 2). The  
 280 tides in this system are dominated by the semi-diurnal M2 tidal constituent, with stronger and  
 281 weaker spring-neap tides each lunar month due to the semi-diurnal S2 and N2 tidal constituents.  
 282 During the study period, stronger spring tides occurred in early October and early November. A  
 283 storm event in late October caused the subtidal water level to increase by 0.7 m during the  
 284 weak neap tide and increased the freshwater discharge from background levels of 0 – 5 m<sup>3</sup>/s to a  
 285 peak of 30 m<sup>3</sup>/s.

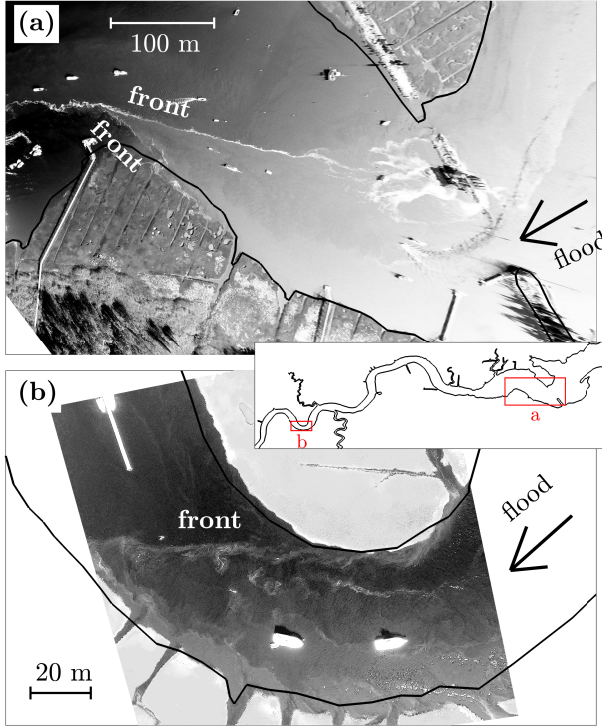


278 FIG. 2. **(a)**: North River discharge in October and November 2021. **(b)** - **(d)**: the modeled estuarine conditions  
 279 compared with observations at the mooring site near the constriction (around 2 km into the estuary). Red lines  
 280 represent model results and dashed black lines represent observations. **(b)**: Water level  $\eta$ . **(c)**: Depth-averaged  
 281 velocity  $\bar{u}$ . Negative  $u$  means landward velocity (flood direction). **(d)**: Depth-averaged salinity  $\bar{s}$ . Gray bands  
 282 show the tidal cycle selected for detailed analysis. Additional model-data comparisons are provided in the  
 283 Supplemental Material.

292 The salinity and stratification varied at tidal time scales at the mooring locations. The tidal  
 293 maximum stratification (bottom-surface salinity difference) was typically 5 – 10 psu, and was up  
 294 to 20 psu during the high discharge event (not shown).

295 *b. Drone imagery of surface fronts*

299 In this section, we present drone imagery of surface fronts at two locations during spring flood  
 300 tides in October and November, 2021. These observational results are primarily explained at a



296 FIG. 3. Drone imagery during spring flood tides. **(a)**: The constriction region at around 2 km into the estuary,  
 297 at 11 am on Oct 7, 2021. **(b)**: A bend at around 5.5 km into the estuary (bend2 in Fig. 1), at 12 pm on Oct 8,  
 298 2021. Locations of the surveyed constriction and bend are shown by red rectangles on the map.

301 descriptive level to demonstrate the motivation for this study, and a more thorough analysis is  
 302 conducted in the numerical model study in the following sections.

303 A V-shaped tidal intrusion front occurred downstream (landward) of the constriction at around  
 304 2 km into the estuary, as is shown in the drone imagery in Fig. 3 **(a)**. The tidal flow through the  
 305 constriction intruded into the ambient, lower salinity water downstream of the constriction, leading  
 306 to a V-shaped surface convergence zone with white foam accumulated on the surface. Higher  
 307 velocities inside the V-shape brought higher salinity water landward through differential advection  
 308 and created sharp salinity gradients across the V-shaped front.

309 Another example of surface fronts is shown in the drone imagery from a bend at around 5.5 km  
 310 into the estuary (Fig. 3 **(b)**, bend2 in Fig. 1). Flow separation occurred in the bend as a result of  
 311 the curvature effect (Bo et al. 2021), with a low-velocity separation zone along the inner bank and  
 312 higher streamwise velocities shifted toward the outer bend. Correspondingly, salinity was greater

313 in the outer part of the bend as a result of differential advection. This lateral salinity gradient  
314 consequently formed an oblique surface front that could accumulate foam and debris, as seen in  
315 the drone image (Fig. 3 (b)).

316 Detailed analysis of frontal dynamics will be presented in the following model investigation.  
317 Note that here the bend with drone imagery is located around 5.5 km into the estuary (bend2 in  
318 Fig. 1), whereas the bend selected for model analysis is at around 4 km (bend1 in Fig. 1). We  
319 have selected the bend at 4 km for model analysis because it exhibits stronger surface convergence  
320 and mixing than found in other bends, but the frontal processes are broadly similar in the different  
321 bends.

322 *c. Surface fronts and secondary circulation*

323 In this section, we analyze the tidal intrusion fronts and associated secondary circulation at  
324 a constriction and a bend in the numerical model. At both locations, flow separation occurs  
325 and creates lateral salinity gradients through differential advection. The lateral salinity gradients  
326 thus lead to secondary circulation in the cross-section, which interacts with the salinity field and  
327 contributes to frontogenesis. The following analysis focuses on a stronger spring tide on November  
328 5 as a representative of spring tide conditions when the surface fronts are most noticeable in the  
329 observations and in the model results.

330 1) THE CONSTRICTION

331 During flood tides, the tidal current is accelerated to over 1 m/s in the main opening as a result  
332 of the lateral constriction. Flow separation occurs on the landward side of the constriction, with  
333 strong lateral shear across the separation zones (Fig. 4). The high-velocity jet advects higher salinity  
334 water to landward of the main opening, while lower salinity water remains in the adjacent low-  
335 velocity zone. This differential advection creates sharp horizontal salinity gradients along with the  
336 strong lateral shear. Moreover, surface convergence occurs due to baroclinicity resulting from the  
337 horizontal salinity gradient and two V-shaped surface fronts form downstream of the constriction  
338 (F1 and F2 in Fig. 4). The smaller V-shaped surface convergence front (F1) is attached to the  
339 narrow opening and the larger V-shaped front (F2) is over the shallow shoal farther downstream.

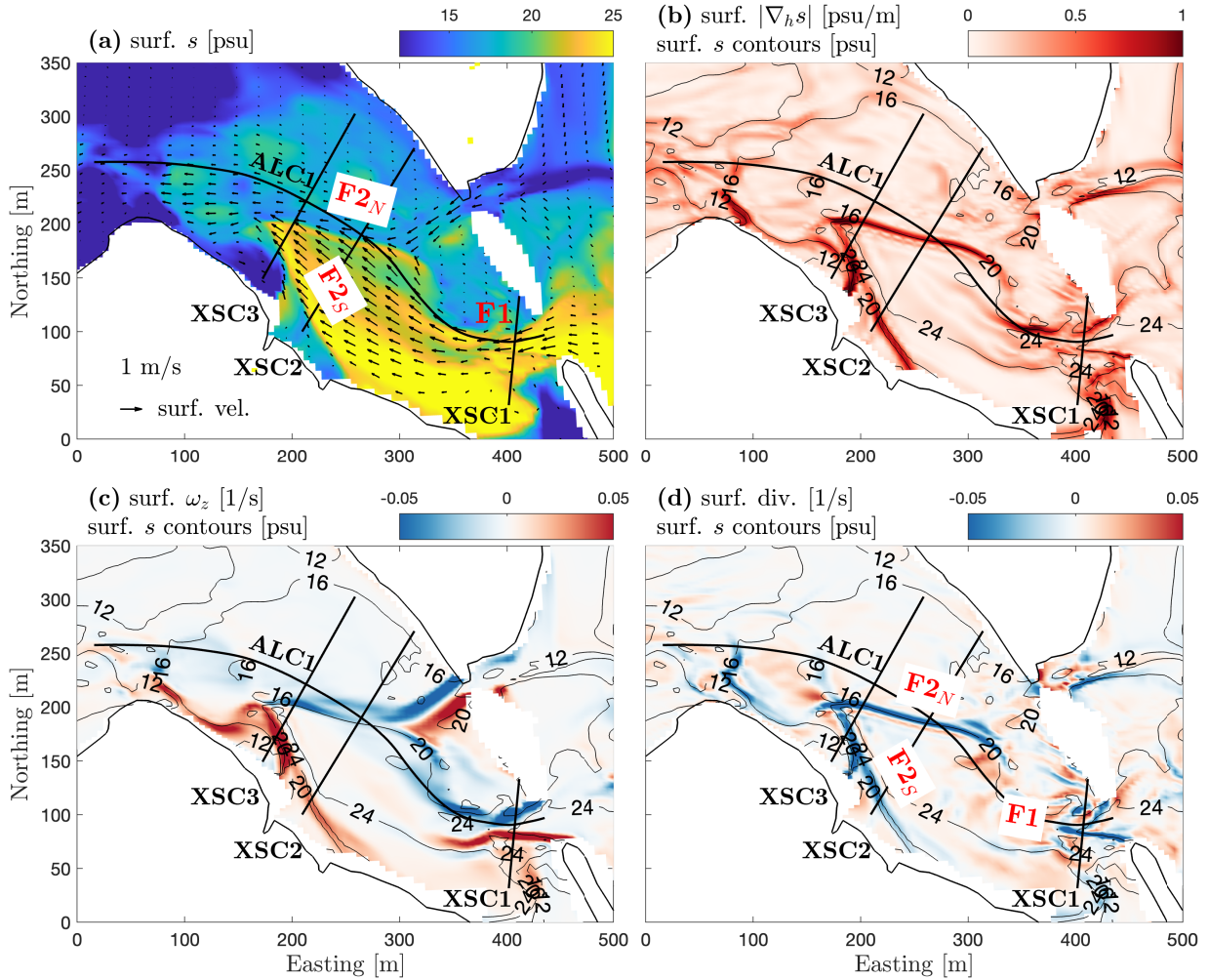


FIG. 4. Flow field in the constriction region at around 2 hours into the flood tide. (a): Surface salinity. Arrows show surface velocity. (b): Horizontal gradients of surface salinity, with contours of surface salinity. (c): Vertical vorticity  $\omega_z$  near the surface (curl of surface horizontal velocity). (d): Divergence of surface velocity, and blue colors represent surface convergence. Black lines show locations of the cross-sections XSC1-3 and the along-channel section ALC1 taken for detailed analysis. The along-channel section is determined based on the streamline of the depth-averaged velocity, and the cross-sections are orthogonal to the streamline. The red “F1” in (a) and (d) marks the smaller V-shaped surface convergence front at the constriction, and “F2<sub>N</sub>” and “F2<sub>S</sub>” mark the north and south sides of the larger V-shaped surface convergence front landward of the constriction.

In a cross-section through the V-shaped front at the constriction (XSC1 in Fig. 5), the jet flow brings higher salinity to the central channel, with a pair of lateral fronts on both sides due to flow separation. The salinity gradients across these lateral fronts lead to a pair of counter-rotating

secondary circulation cells. The circulation cell on the north side has southward velocity near the surface and northward velocity near the bed and the cell on the south side has an opposite sense of circulation. As a result, a surface convergence zone occurs near the center of the cross-section, which corresponds to the V-shaped front F1 near the constriction in the map view (Fig. 4).

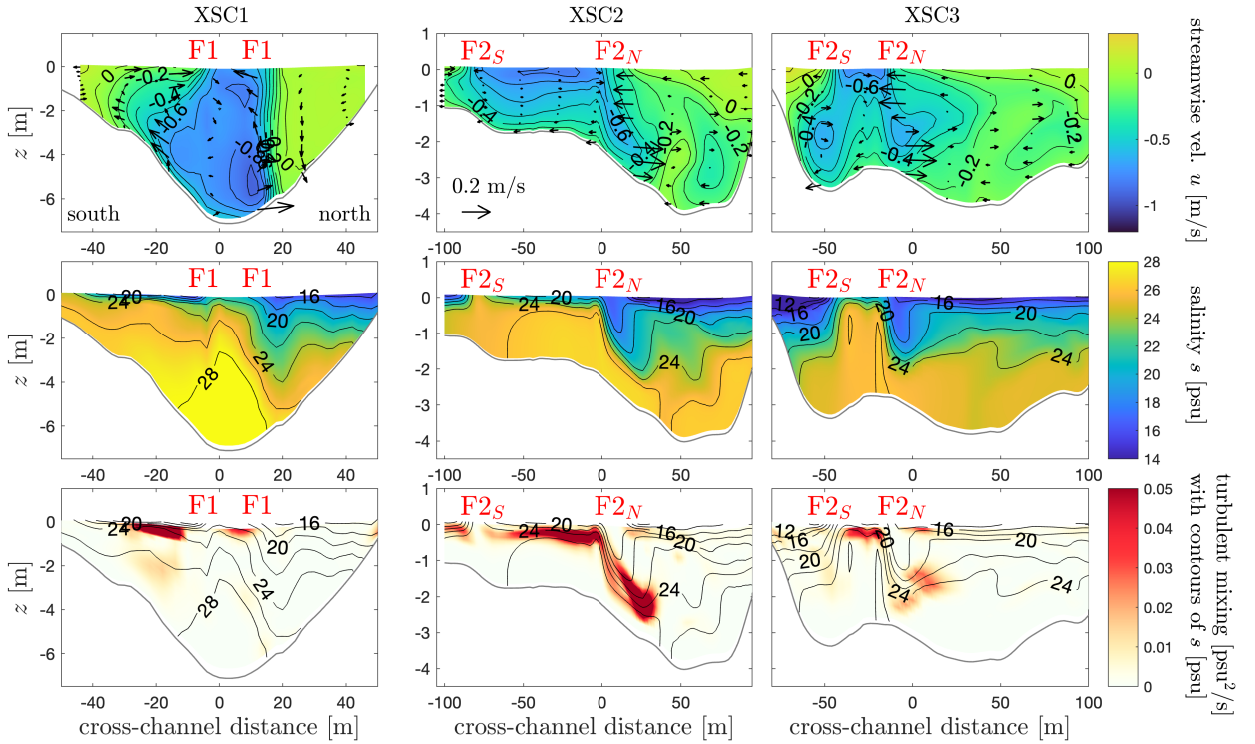
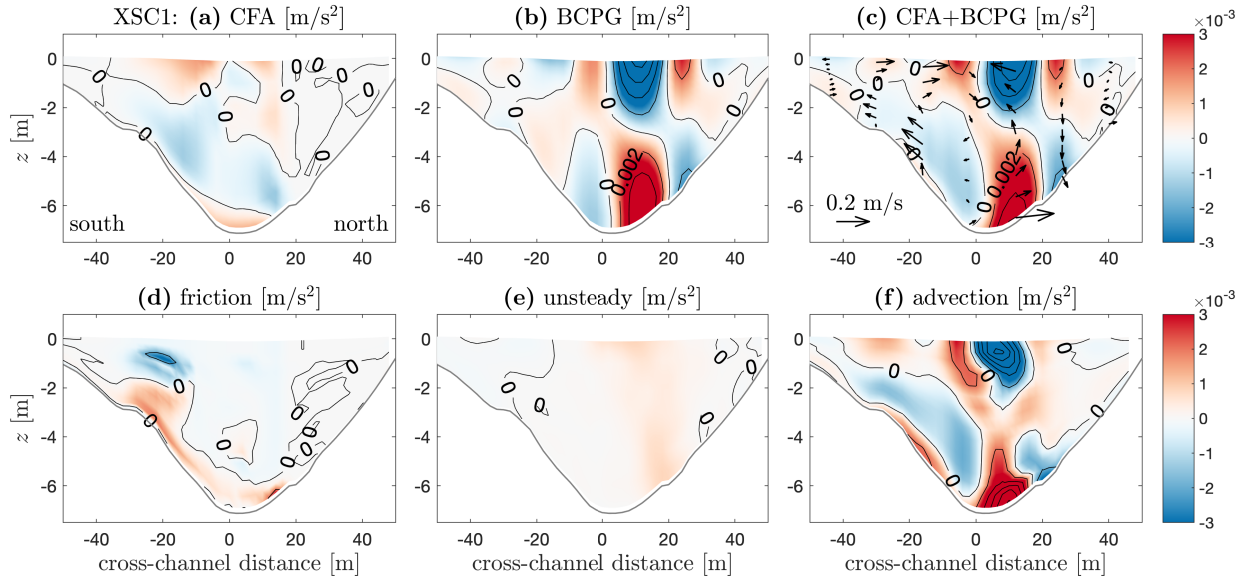


FIG. 5. Streamwise velocity  $u$ , salinity  $s$ , and mixing in cross-sections XSC1, XSC2, and XSC3. Locations of cross-sections are shown in the map views in Fig. 4. Negative  $u$  means landward velocity (flood direction). The southern bank is on the left side, with the flood current going into the page. Arrows show secondary circulation. Locations of the V-shaped surface convergence zones are marked by the red “F1”, “F2<sub>N</sub>”, and “F2<sub>S</sub>”.

We examine the lateral momentum balance (3) in XSC1 to investigate the dynamics of the secondary circulation pattern (Fig. 6). The baroclinic pressure gradient (BCPG) associated with the lateral density variability is the dominant term in driving the pair of counter-rotating circulation cells. The centrifugal acceleration (CFA) is less important since the curvature effect is relatively weak here. The frictional effect is weak in the channel center and increases on the shallower south side of the channel. Instead of friction, the BCPG is mainly balanced by the advection term (downstream adjustment of secondary circulation) in this strongly advective system, consistent with

366 Nidzieko et al. (2009) and Kranenburg et al. (2019). Given the dominance of BCPG in the lateral  
 367 momentum balance, the secondary circulation is thus called BCPG-driven secondary circulation.



368 FIG. 6. Terms in the lateral momentum balance (3) in the cross-section XSC1. Red colors mean northward  
 369 (rightward) forcing, and blue colors mean southward (leftward) forcing.

370 Farther landward, the jet flow expands as it encounters the shallower region downstream from  
 371 the constriction (Fig. 1 and Fig. 4), and the two BCPG-driven secondary circulation cells and the  
 372 corresponding surface convergence zones are separated farther apart (XSC2 in Fig. 5). Secondary  
 373 circulation redistributes streamwise velocity in the cross-section. Taking the lateral front in the  
 374 northern part of XSC2 (front  $F_{2N}$ ) as an example, the laterally sheared streamwise flow, with  
 375 weaker velocity on the north side, is twisted into vertical shear by the counterclockwise secondary  
 376 circulation. This downward and northward intrusion of high streamwise momentum leads to a  
 377 reversal in vertical shear, with lower velocity in the upper water column. The BCPG-driven  
 378 secondary circulation also laterally transports salinity near the front, with the near-bottom lateral  
 379 flow advecting saltier water northward and the near-surface flow advecting fresher water southward.  
 380 As a result, lateral salinity gradients initially created by differential advection are converted to  
 381 vertical gradients by the secondary circulation, creating stratification through this lateral straining.

382 In addition to the creation of stratification, mixing that acts to destroy stratification also occurs at  
 383 the north-side front in XSC2 (Fig. 5), and the detailed mechanism of mixing will be analyzed in the

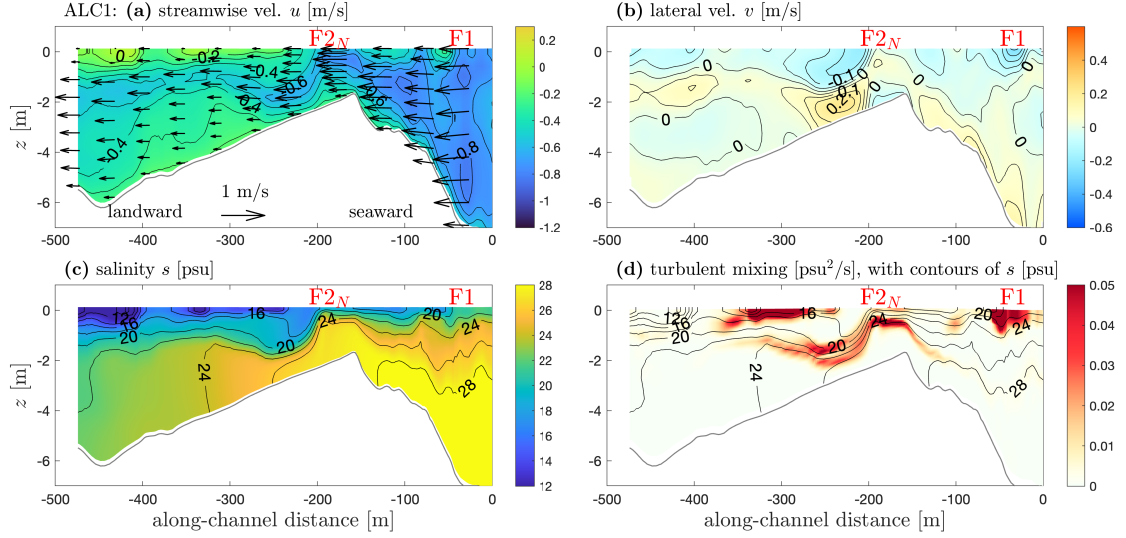
following sections. The front on the north side ( $F2_N$ ) is in deeper water and is more representative of other tidal intrusion fronts in the system. The water column in the southern part of XSC2 is only 1 – 2 m deep (see front  $F2_S$ ), and the greater influence of the bottom boundary leads to different mechanisms of frontal dynamics, which will be discussed later.

The pair of lateral surface fronts ( $F2_N$  and  $F2_S$ ) converge near the center of the jet flow (e.g., comparing XSC2 and XSC3). The surface convergence zones are oblique to the streamwise current and form the second, larger V-shaped tidal intrusion front (Simpson and Nunes 1981; Largier 1992) (Fig. 4). The composite Froude number  $G$  for two-layer flow (e.g., Armi and Farmer 1986; Geyer and Ralston 2015) is examined to understand the oblique angle of the front.

$$G^2 = \frac{u_1^2}{g'H_1} + \frac{u_2^2}{g'H_2}, \quad (12)$$

where  $u_1$  and  $u_2$  are the average velocities of the upper and lower layers, and  $H_1$  and  $H_2$  are the layer thickness.  $g' = g(\Delta\rho/\bar{\rho})$  is the reduced gravity based on the density difference between the two layers. The composite Froude number based on the streamwise layer velocities is  $G \approx 3$  at the front  $F2$ , indicating a supercritical condition. Nevertheless, the front is relatively stationary during several hours in the flood tide rather than moving landward with flood tidal currents. A stationary front can occur under a supercritical condition when it is oblique to the main flow direction such that the critical condition is satisfied in the direction normal to the front (Largier 1993; MacDonald and Geyer 2005; Geyer and Ralston 2015). In this case, the front  $F2$  has an oblique angle  $\phi \approx 20^\circ$ , so that the front-normal Froude number  $G \sin \phi$  is close to 1, the critical condition.

Note that while tidal currents are usually slower over shallow regions due to topographic steering (e.g., Dietrich and Smith 1983), in this case, currents over the shoal inside of the V-shaped front  $F2$  are faster than in the deeper region to the north. This demonstrates that the lateral shear across front  $F2$  is associated with the jet flow from the narrow opening rather than due to topographic steering and the bottom frictional torque. As the jet flow transitions from the shallow shoal into deeper water, the composite Froude number decreases. A relatively stationary front is maintained at the channel-shoal transition where the composite Froude number decreases to the critical value of 1, with the oblique flow angle incorporated (front  $F2_N$  in Fig. 7). The flooding streamwise flow of higher salinity water subducts when encountering the surface front. The surface convergence



402 FIG. 7. The along-channel section ALC1 (location shown in Fig. 4). **(a)**: Streamwise velocity  $u$ . **(b)**: Lateral  
403 velocity  $v$ . Positive  $v$  is northward. **(c)**: Salinity  $s$ . **(d)**: Mixing, with contours of  $s$ . The red “F1” and “F2<sub>N</sub>”  
404 show the locations of the V-shaped surface convergence zones. Negative distance means landward direction, and  
405 the constriction opening is at 0 m.

415 at the front mainly results from the lateral circulation, but the streamwise flow that encounters the  
416 oblique front enhances the convergence at the surface as well.

417 While the V-shaped convergence zone on the surface is prominent both in the model and in the  
418 field, the flow and salinity fields associated with the tidal intrusion front are strongly 3-d (see the  
419 cross-sections in Fig. 5 and the along-channel section Fig. 7). The V-shaped surface convergence  
420 zone and 3-d frontal structure are also generally consistent with observations from drone imagery  
421 (Fig. 3 **(a)**) and shipboard measurements (see Appendix A). Note that the snapshot in the model  
422 results corresponds to an earlier tidal stage (2 hours into the flood, Fig. 4) than the drone imagery  
423 (3 hours into the flood, Fig. 3). We provide a model snapshot from later in the tide that is similar to  
424 the V-shaped front observed in the drone imagery in Appendix B (Fig. B1). The earlier snapshot  
425 is selected for detailed analysis because of the presence of stronger mixing at that time.

426 To summarize the frontal dynamics in the constriction region, flow separation occurs downstream  
427 of the narrow opening, with strong shear across the separation zones. The laterally sheared flow  
428 leads to the formation of sharp lateral salinity gradients through differential advection, resulting in  
429 lateral fronts. Secondary circulation occurs near the fronts driven by the baroclinic forcing. The

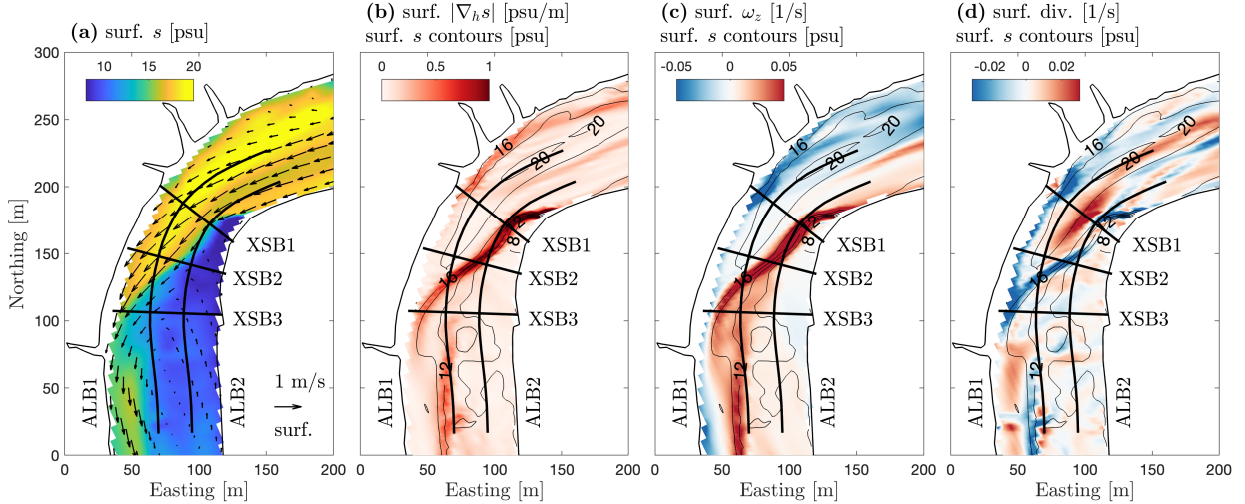
secondary circulation both enhances the stratification and leads to intense mixing near the front, as will be analyzed in detail later. Secondary circulation also influences the horizontal velocity convergence, which can cause additional feedback on frontogenesis. The subsequent analysis of this study (sections 3 d and 3 e) focuses on the stratification and mixing associated with the front rather than the detailed interactions between frontogenesis and velocity convergence. In addition to this sharp constriction at the railroad embankment, similar tidal intrusion fronts also occur during the flood tide at other topographic features along the estuary where flow separation occurs, e.g., sand spits, island shoals, and in meanders (Appendix B and section 3 c 2).

## 2) THE BEND

In the bend at around 4 km (bend1 in Fig. 1 (b)), a surface front occurs as a result of flow separation and differential advection. The channel flow detaches from the inner bank at the bend apex, with a low-velocity separation zone formed near the inner bank in the lee of the bend (Fig. 8). The main flow is accelerated in the outer bend as it is restricted to a narrower part of the channel due to flow separation. As a result, salinity is higher near the outer bank and lower near the inner bank due to the differential advection of the along-estuary salinity gradient, leading to a sharp lateral front at the boundary of the separation zone.

In general, a single secondary circulation cell occurs in the cross-section (Fig. 9) with outward velocity in the upper water column and inward velocity in the lower column. The lower salinity near the inner bank and higher salinity near the outer bank create BCPG forcing that is outward near the surface and inward near the bottom (e.g., at cross-channel distance of 0 m in XSB1 in Fig. 10), and this BCPG drives the counterclockwise secondary circulation. In addition, the CFA due to the curvature effect has comparable magnitude to the BCPG and a similar tendency to drive counterclockwise secondary circulation, with outward forcing near the surface and inward forcing near the bottom at 0 m cross-channel distance in XSB1.

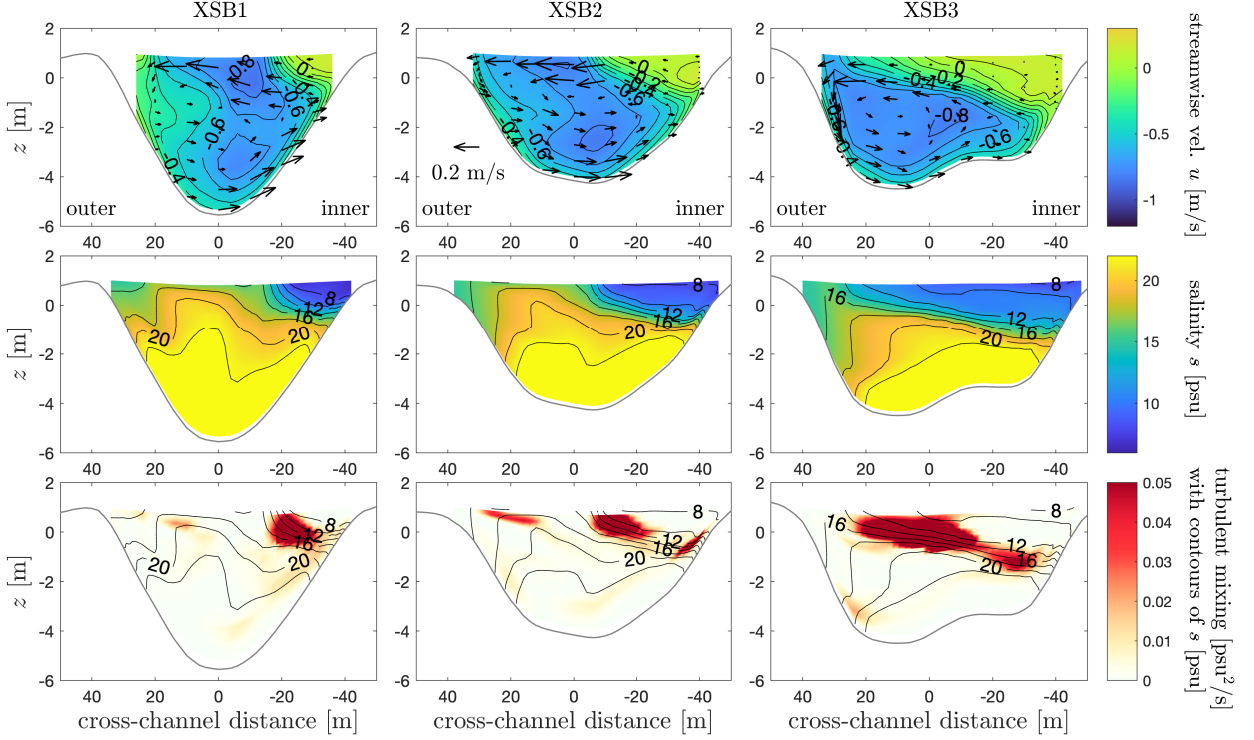
The counterclockwise secondary circulation laterally transports lower salinity toward the outer bank near the surface (Fig. 9), so that the lateral surface front exhibits an oblique angle to the along-channel direction, spanning from the inner bank of the bend apex to the downstream outer bank (Fig. 8). In addition, the vertically-sheared lateral velocity strains lateral salinity gradients into vertical gradients and thus increases stratification (Fig. 9). Likewise, secondary circulation also



446 FIG. 8. Flow field in the bend region at around 3 hours into the flood tide. **(a)**: Surface salinity. Arrows show  
 447 surface velocity. **(b)**: Horizontal gradients of surface salinity, with contours of surface salinity. **(c)**: Vertical  
 448 vorticity  $\omega_z$  near the surface (curl of surface horizontal velocity). **(d)**: Divergence of surface velocity, and blue  
 449 colors represent surface convergence. Black lines show locations of the cross-sections and along-channel section  
 450 taken for detailed analysis. The along-channel and cross-channel coordinates are established with reference to  
 451 lines that are parallel and orthogonal to the channel centerline.

469 affects the distribution of streamwise velocity in the cross-section. The slower-velocity separation  
 470 zone expands outward near the surface, leading to slower velocity on top of faster velocity in the  
 471 water column, i.e., the twisting of lateral shear into reversed vertical shear by the counterclockwise  
 472 secondary circulation. Intense turbulent mixing occurs in the upper water column at the frontal  
 473 boundary (Fig. 9), and the mechanism of mixing will be analyzed in the following sections along  
 474 with that in the constriction region.

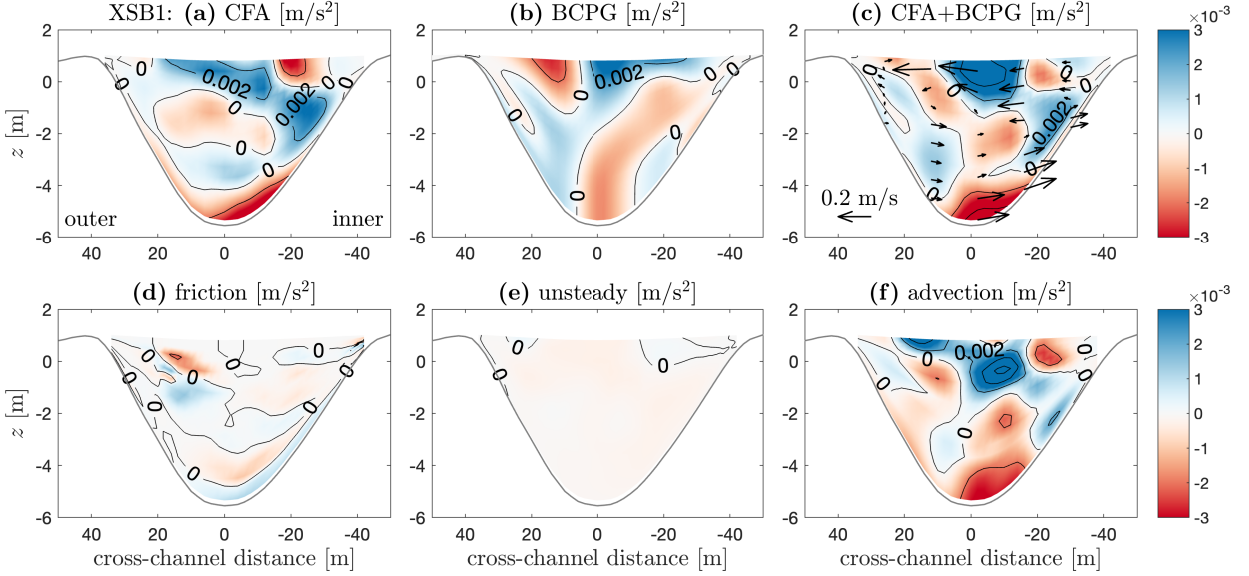
480 As the reversed vertical shear of streamwise velocity grows in the separation zone, i.e., slower  
 481 velocity on top of faster velocity, the sense of CFA forcing is reversed in the lateral momentum  
 482 budget (e.g., at -20 m cross-channel distance in XSB1 in Fig. 10, inward near the surface and  
 483 outward in the lower column). This reversed CFA may reverse the sense of secondary circulation  
 484 within the separation zone, leading to weak inward lateral velocity at the surface and outward  
 485 velocity in the middle water column (e.g., at -40 to 0 m in XSB3 in Fig. 9). The reversal of CFA  
 486 and secondary circulation in the separation zone is consistent with analysis of previous observations  
 487 in this estuary (Kranenburg et al. 2019). The smaller, reversed (clockwise) secondary circulation



460 FIG. 9. Streamwise velocity  $u$ , salinity  $s$ , and mixing in cross-sections XSB1, XSB2, and XSB3. Locations  
 461 of cross-sections are shown in Fig. 8. Arrows show secondary circulation. Negative  $u$  means landward velocity  
 462 (flood direction). The inner bank is on the right side, with the flood current coming out of the page. Note that in  
 463 these cross-sections, + $y$  is leftward (outward) to ensure a right-hand coordinate system.

488 cell at the inside of the bend has a weak tendency to decrease stratification in the separation zone, in  
 489 contrast to the salinity straining and increased stratification associated with the counterclockwise  
 490 secondary circulation on the outer side of the flow separation front. In addition, the reversed  
 491 secondary circulation in the separation zone tends to convert vertical shear back to lateral shear,  
 492 opposite to the shear twisting effect of the major counterclockwise secondary circulation.

493 The reversal of CFA in the separation zone tends to create surface divergence near the front (e.g.,  
 494 at 0 m to -20 m cross-channel distance in XSB1 in Fig. 10), counteracting the surface convergence  
 495 due to the baroclinic effect at the front. The competing influences of the curvature effect (CFA) and  
 496 the baroclinic effect is reflected in the discrepancy between surface horizontal salinity gradients  
 497 and the surface convergence patterns downstream of the bend in the map view (Fig. 8). While  
 498 generally surface convergences are correlated with sharp horizontal salinity gradients through

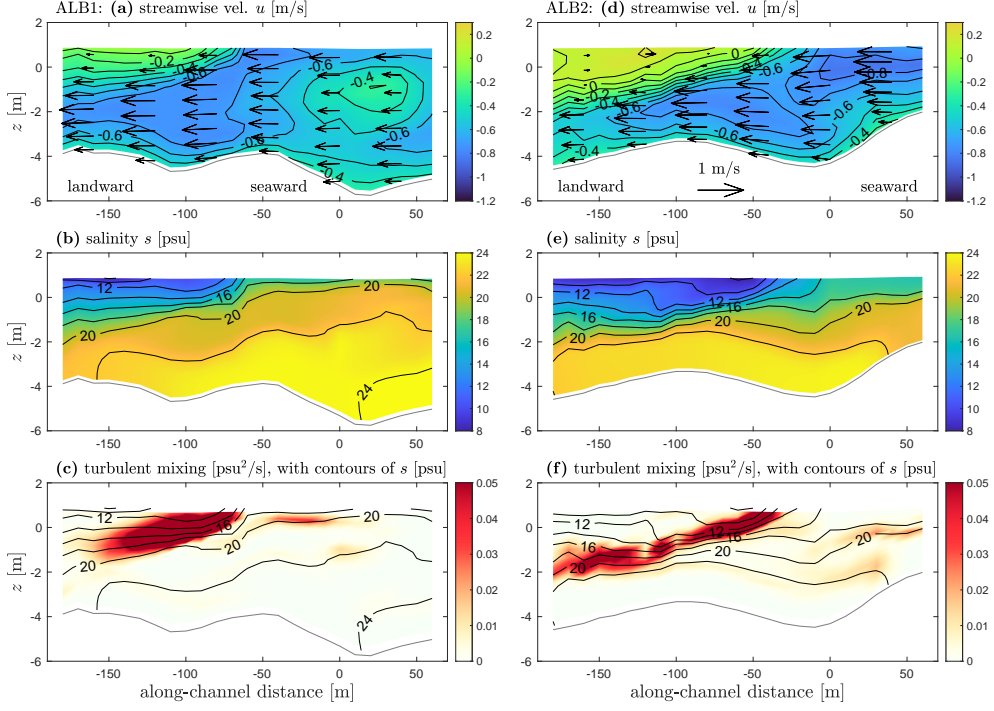


475 FIG. 10. Terms in the lateral momentum balance (3) in the cross-section XSB1. The flood current is out of  
 476 the page, and the inner bank is on the right side. Red colors mean inward (rightward) forcing, and blue colors  
 477 mean outward (leftward) forcing. The advection term is placed on the left side of (3), so the momentum balance  
 478 is achieved when the total forcing terms on the right side, primarily CFA and BCPG, equal the advection term.  
 479 Note that here a positive value of forcing means leftward, because  $+y$  is leftward (also see Fig. 9).

499 baroclinicity, surface divergence occurs where the curvature effect locally exceeds the baroclinic  
 500 effect, particularly near the bend apex.

501 Overall, the frontal dynamics, secondary circulation, and mixing in the bend region share  
 502 similarities to the constriction region in that: (1) a tidal intrusion front (surface convergence,  
 503 Fig. 8) occurs due to flow separation; (2) the front is relatively stationary and has an oblique angle  
 504 to the main channel flow direction; (3) secondary circulation strains the lateral salinity gradient  
 505 and creates stratification (Fig. 9); (4) secondary circulation twists the laterally sheared streamwise  
 506 flow at the lateral front and leads to reversed vertical shear in the upper water column; (5) intense  
 507 near-surface mixing occurs at the salinity front at the boundary of the flow separation zone (Figs. 9  
 508 and 11).

512 One major difference between the bend and the constriction is the mechanism of flow separation.  
 513 In the constriction region, flow separation occurs on both sides of the jet flow from the narrow  
 514 opening. In the bend, flow separation only occurs near the inner bank downstream of the bend apex



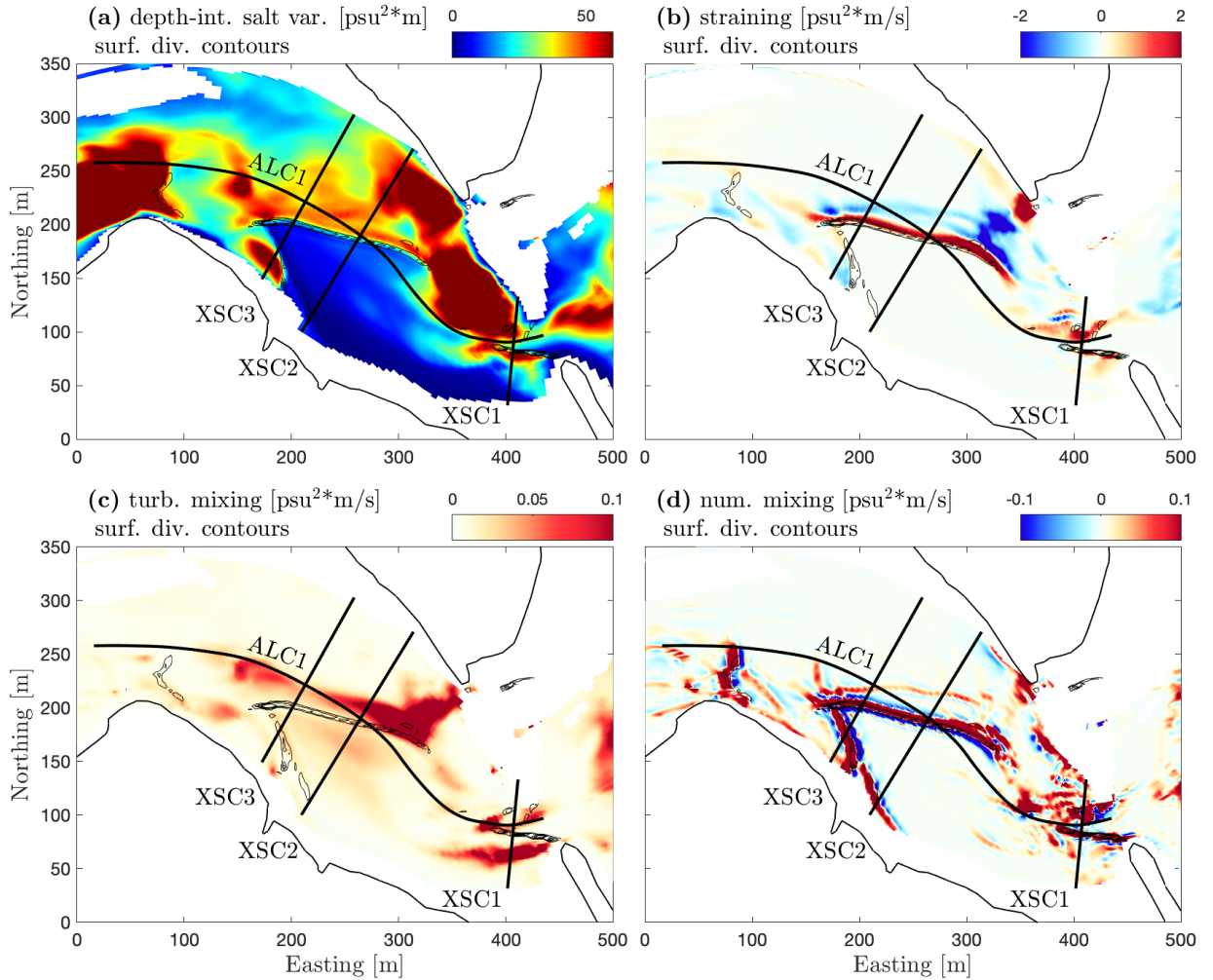
509 FIG. 11. Streamwise velocity  $u$ , salinity  $s$ , and mixing in along-channel sections ALB1 and ALB2. Locations  
 510 of ALB1 and ALB2 are shown in Fig. 8. Negative distance means landward direction, and the bend apex is at  
 511 0 m.

515 due to the channel curvature effect (Leeder and Bridges 1975; Blanckaert 2015; Bo and Ralston  
 516 2020). As a result, a single surface front is created in the bend and instead of two fronts converging  
 517 in a V-shape as with the constriction. The fronts in both cases are oriented at an angle to the  
 518 channel due to the Froude number constraint, so essentially the bend front resembles half of the  
 519 V-shape of the tidal intrusion at the constriction (Fig. 8).

520 Another major difference between the bend and the constriction lies in the driving force for  
 521 secondary circulation in the lateral momentum balance (3) (XSB1 in Fig. 10). While the BCPG  
 522 dominates over CFA in the constriction region, both terms are important for the lateral momentum  
 523 balance in the bend. In the bend, both CFA and BCPG act to drive the counterclockwise secondary  
 524 circulation near the lateral front, and CFA also creates a smaller reversed (clockwise) secondary  
 525 circulation cell in the separation zone. The additional CFA forcing due to channel curvature  
 526 may create surface divergence near the front and thus act against the frontogenesis tendency of

527 baroclinicity. The occurrence of reversed secondary circulation also adds complexity to the lateral  
 528 salinity straining and shear twisting processes.

529 *d. Quantifying mixing and straining*



530 FIG. 12. Terms in the vertical salinity variance budget (11) in the constriction region. **(a)**: Depth-integrated  
 531 salinity variance, with contours of surface divergence. **(b)**: Depth-integrated straining. **(c)**: Depth-integrated  
 532 turbulent mixing. **(d)**: Depth-integrated numerical mixing. For mixing and numerical mixing, positive values  
 533 (red colors) stand for destruction of stratification; for straining, positive values (red colors) stand for creation of  
 534 stratification. Note the different color ranges of mixing and straining. The local magnitude of turbulent mixing  
 535 can be much smaller than numerical mixing and straining, but their spatially-integrated effects are comparable  
 536 in the variance budget.

537 The vertical salinity variance budget (11) is calculated to quantitatively understand the influences  
538 of straining and mixing associated with surface fronts on stratification. In the constriction region,  
539 strong positive straining is found at the V-shaped tidal intrusion front, causing an increase in  
540 stratification (Fig. 12 **(b)**). Locally, the straining term is dominantly due to the lateral component in  
541 (11), i.e., the interaction between vertical variations of lateral velocity and lateral salinity gradients.  
542 This positive straining in the variance budget converts lateral gradients to stratification through  
543 the BCPG-driven secondary circulation at the front (see the cross-sectional plots in Fig. 5). Note  
544 that some negative straining occurs north of the V-shaped front. This is because the downward  
545 velocity of secondary circulation locally suppresses the pycnocline and creates weak lateral salinity  
546 gradients north of the downwelling region, with higher salinity north of lower salinity (e.g., in the  
547 north part of XSC2 and XSC3 in Fig. 5)). Negative straining occurs as the BCPG-driven lateral  
548 flows twist these weak lateral salinity gradients north of the front. Overall, positive straining at the  
549 front is much larger than negative straining north of the front, and the net effect of straining is to  
550 increase stratification.

551 While the positive straining at the tidal intrusion front is a source of stratification, the strong  
552 turbulent mixing near it tends to destroy salinity variance (Fig. 12 **(c)**). Turbulent mixing is  
553 increased near the front due to the vertical shear and increased eddy diffusivity from the turbulence  
554 closure. While the strongest positive straining is collocated with the surface convergence front in  
555 the map view, the strongest turbulent mixing is adjacent to the convergence zone, outside of the  
556 V-shape. This reflects the 3-d structure of the front, as most of the turbulent mixing occurs away  
557 from the surface convergence where the frontal boundary extends into the water column (Figs. 5  
558 and 7).

559 Additional dissipation of salinity variance occurs due to numerical mixing at the surface con-  
560 vergence zone where salinity gradients are sharpest (Fig. 12 **(d)**). Numerical mixing can locally  
561 be either positive or negative, but the integration of numerical mixing is usually positive, i.e.,  
562 an overall effect to decrease stratification. Numerical mixing results from the discretized tracer  
563 advection scheme in the model (Burchard and Rennau 2008). Generally, numerical mixing pro-  
564 vides a proxy for the turbulent mixing that would happen in an actual frontal zone, where some  
565 salinity gradients occur within the grid scale and therefore cannot be resolved in the model (Ralston  
566 et al. 2017). Nevertheless, the consistency between model and observations (sections 3 b and 3 c

and Appendix A) indicates that numerical mixing provides a necessary contribution to the overall dissipation of salinity variance to yield realistic salinity fields.

Spatially integrating the variance budget over the constriction region, straining (mostly lateral straining) is the dominant source of stratification during the flood tide. The created stratification is destroyed by the combination of turbulent mixing (60%) and numerical mixing (40%). Note that the total mixing generally balances with straining in the spatially and temporally integrated variance budget, but mixing and straining are not balanced locally and instantaneously, which thus leads to rapid creation or destruction of stratification near frontal zones.

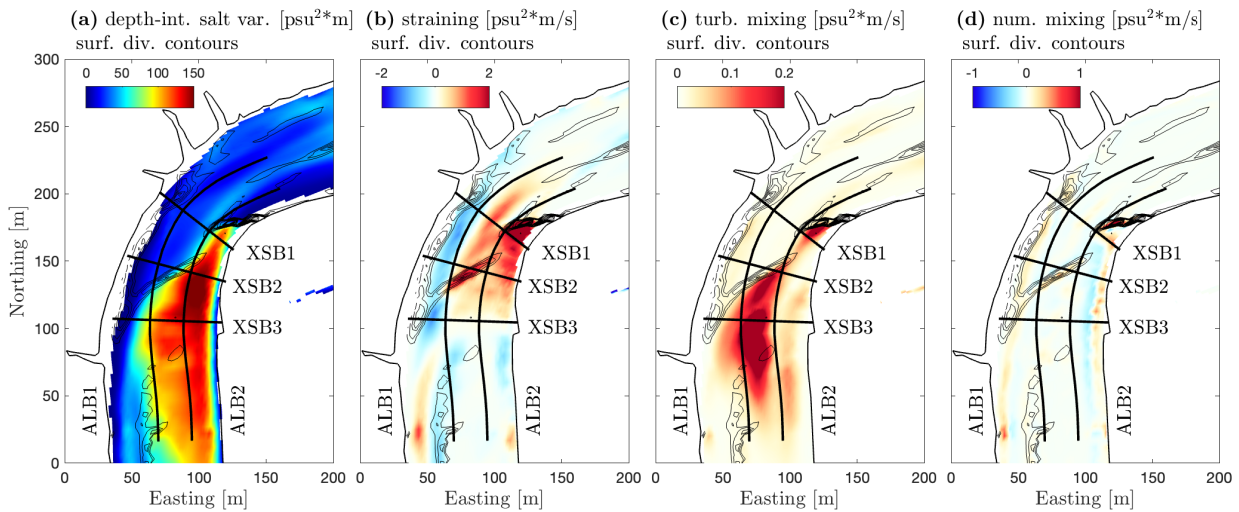


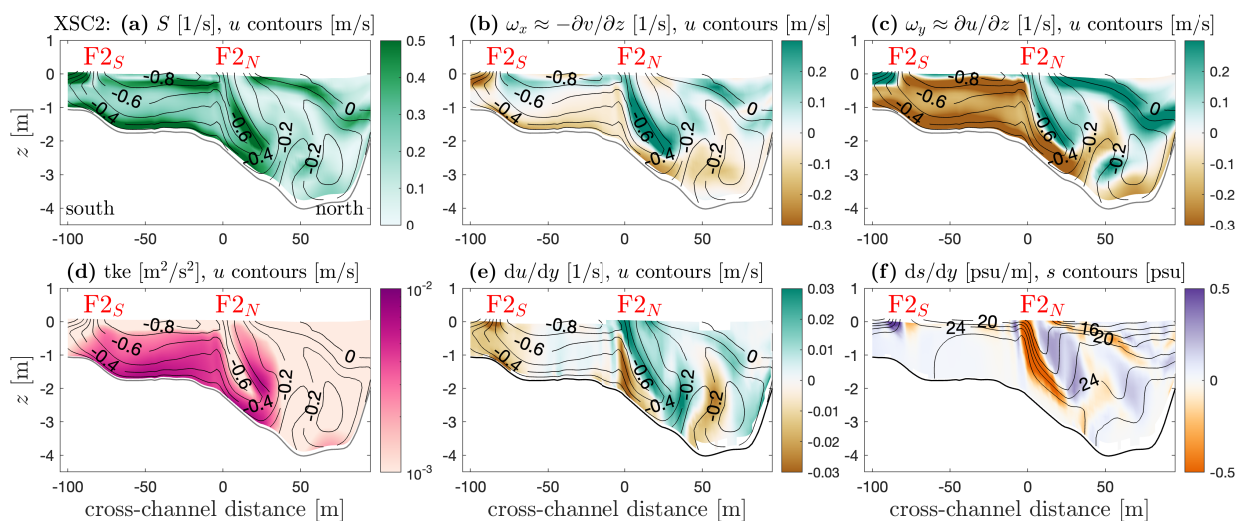
FIG. 13. Terms in the vertical salinity variance budget (11) in the bend region. **(a)**: Depth-integrated salinity variance, with contours of surface divergence. **(b)**: Depth-integrated straining. **(c)**: Depth-integrated turbulent mixing. **(d)**: Depth-integrated numerical mixing.

In the bend region, straining and mixing have similar patterns as in the constriction. Intense positive straining occurs at the surface convergence front (Fig. 13 **(b)**), which represents the creation of stratification by secondary circulation (see cross-sectional plots in Fig. 9). Regions with strong turbulent mixing are offset from the surface convergence zone in the map view (Fig. 13 **(c)**), which corresponds to the enhanced mixing at the inclined, subsurface frontal zone (Figs. 9 and 11). Numerical mixing is weaker in the bend region compared to the constriction region. This is likely due to the less oblique front angle and the lower front-normal velocities in the bend, corresponding to weaker convergence and weaker horizontal salinity gradients. As a result, turbulent mixing accounts for 80% of the total mixing in the bend.

587 While the straining of salinity and creation of stratification associated with surface fronts has been  
 588 reported in estuaries (e.g., Largier 1992; O'Donnell 1993; Giddings et al. 2012), the co-occurring  
 589 mixing has received less attention. Our analysis suggests that strong turbulent mixing can happen  
 590 near the surface convergence zone and tends to destroy the stratification created by straining. The  
 591 horizontal salinity gradient across the front drives secondary circulation, which interacts with the  
 592 salinity field to create stratification and with the streamwise velocity to create shear and turbulence.  
 593 The occurrence of mixing near the front thus depends on the competition between these two  
 594 processes, and the detailed mechanism of mixing will be examined in the following section.

595 *e. Stability and mixing at the front*

596 In this section, we investigate the dynamical processes that lead to turbulent mixing near the tidal  
 597 intrusion front. The north-side front in XSC2 (at cross-channel distance of 0 to 50 m, the northern  
 598 part of the V-shaped front  $F2_N$ ) in the constriction region is selected as an example. Vertical shear  
 599 is enhanced at the front (Fig. 14 (a)), which provides a source of turbulence generation (Fig. 14 (d))  
 600 and mixing (Fig. 5 XSC2). The enhanced vertical shear results from both the shear of lateral flow  
 601 (longitudinal vorticity  $\omega_x$ ) and the shear of streamwise flow (lateral vorticity  $\omega_y$ ) (Fig. 14 (b), (c)).



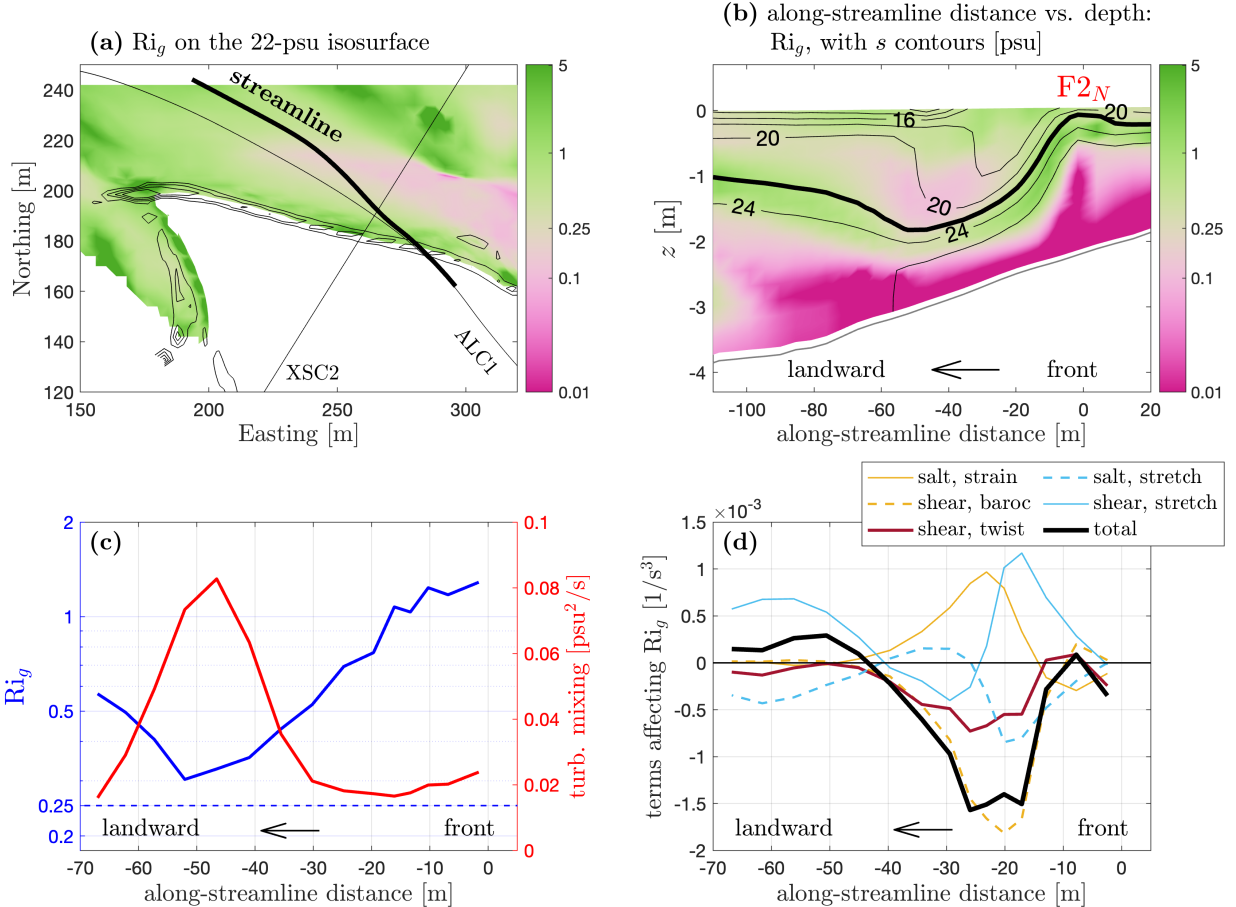
602 FIG. 14. (a): Total vertical shear  $S$  in the cross-section XSC2, with contours of streamwise velocity. (b):  $\omega_x$   
 603 (vertical shear of lateral velocity). (c):  $\omega_y$  (vertical shear of streamwise velocity). (d): Turbulent kinetic energy  
 604 tke. (e): Lateral shear of streamwise velocity. (f): Lateral salinity gradient, with contours of salinity  $s$ .

605 The vorticity equations (5) are examined to understand the factors contributing to the vertical  
606 shear. The positive longitudinal vorticity  $\omega_x$  at the front corresponds to the counterclockwise  
607 BCPG-driven secondary circulation downstream of the constriction.  $\omega_x$  is primarily forced by  
608 the lateral salinity gradient (see Fig. 14 (f) and Eq. (5a)), consistent with the momentum balance  
609 analysis where the BCPG is dominant in driving secondary circulation (Eq. (3) and Fig. 6). In  
610 the equation for the lateral vorticity  $\omega_y$  (Eq. (5b)), the vorticity twisting (the third term) is most  
611 important for the creation of  $\omega_y$ . Secondary circulation ( $\omega_x$ ) can twist the laterally sheared  
612 streamwise flow ( $\partial u / \partial y$ , i.e., part of the vertical vorticity, as Fig. 14 (e) shows), and thus generate  
613  $\omega_y$  at the front. The along-channel salinity gradient in (5b) also has a tendency to increase  $\omega_y$ ,  
614 because the front is oblique to the jet flow from the constriction. However, this along-channel  
615 baroclinicity is weak because the orientation of the front is closer to the along-channel direction,  
616 and the lateral shear and lateral baroclinicity are more important.

617 Note that the lateral vorticity  $\omega_y$  is positive at the front (Fig. 14 (c)), and it corresponds to  
618 the reversed vertical shear of the streamwise current, i.e., slower flood current above faster flood  
619 current (also see Fig. 5). In contrast to the bottom boundary layer where the no-slip condition  
620 causes velocity to increase with distance above the bed and creates negative  $\omega_y$ , this reversed shear  
621 provides corroborating evidence that the pattern of shear and mixing is mainly associated with  
622 surface dynamics. Negative  $\omega_y$  (normal shear) is found in the south part of XSC2 (Fig. 14 (c)),  
623 because of the greater influence of the bottom boundary in this shallow region.

636 While strong shear created near the north-side front ( $F2_N$ ) favors turbulence and mixing, strat-  
637 ification is also created there due to the straining of horizontal salinity gradients (section 3 d),  
638 potentially stabilizing the water column and inhibiting turbulence. We examine the  $Ri_g$  tendency  
639 equation (10) following a similar method to Collignon and Stacey (2013) to investigate the overall  
640 influence of frontal dynamics on water column stability.

641 The gradient Richardson number  $Ri_g$  along a streamline through the frontal zone decreases from  
642 greater than 1 at the surface convergence zone to around the critical value  $Ri_{g,cr} \approx 0.25$  at the  
643 subducting frontal zone, thus allowing for turbulence and mixing (Fig. 15 (a)-(c)). Note that the  
644 time derivative of  $Ri_g$  in Eulerian coordinates is small compared to the advection terms, so  $Ri_g$  is  
645 relatively steady in time at the stationary front. The decreasing trend of  $Ri_g$  refers to the Lagrangian



624 FIG. 15. Gradient Richardson number dynamics near the constriction. **(a)**: Gradient Richardson number  $Ri_g$   
625 on the 22-psu salinity isosurface. Black contours of surface convergence show the V-shaped surface front. The  
626 thick black line shows a 3-d streamline with the starting point on the 22-psu isosurface. Note that the streamline  
627 subducts at the surface convergence front and generally follows the 22-psu isosurface. Thin black lines show  
628 the locations of the cross-section XSC2 and the along-channel section ALC1 shown in Figs. 4, 5, and 7. **(b)**:  
629  $Ri_g$  on the along-streamline distance vs. depth plot, with salinity contours. The 22-psu contour is thickened  
630 and it generally corresponds with the 3-d streamline in panel **(a)**. The surface convergence zone is at 0-m  
631 along-streamline distance. **(c)**:  $Ri_g$  and turbulent mixing along the 3-d streamline. Also refer to Fig. 5 XSC2 and  
632 Fig. 7. **(d)**: Terms in the  $Ri_g$  tendency equation (10) along the 3-d streamline, including the salinity straining  
633 and stretching/compressing terms that affect stratification, vertical shear generation due to baroclinicity, vertical  
634 shear generation due to twisting of horizontal shear, vertical shear generation (vortex stretching) associated with  
635 velocity divergence/convergence. See legend for details.

646 coordinates and is mostly associated with advection, i.e., the downstream decrease in  $Ri_g$  along the  
647 streamline.

648 The straining of horizontal salinity gradients, primarily due to lateral straining, creates stratifi-  
649 cation and tends to increase  $Ri_g$  (Fig. 15 (d)). The horizontal salinity gradients also enhance the  
650 vertical shear through baroclinicity (primarily in the lateral direction), and thus tend to decrease  
651  $Ri_g$ . The direct influences of horizontal salinity gradients on stratification and shear, i.e., the first  
652 two right-side terms in (10), have a net tendency to decrease  $Ri_g$  to 0.5 rather than 0.25 (Simpson  
653 and Linden 1989). In addition, the vorticity twisting term contributes to decreasing  $Ri_g$  (the third  
654 term in (10), primarily the twisting of lateral shear into vertical shear) as the laterally sheared  
655 jet flow from the constriction interacts with baroclinic secondary circulation. This tendency to  
656 decrease  $Ri_g$  relates to the creation of reversed shear in the upper water column, as noted in the  
657 vorticity analysis above, and it contributes to around 1/3 of the total decreasing tendency of  $Ri_g$   
658 at the subducting front. The decreasing trend of  $Ri_g$  thus tends to destabilize the water column,  
659 favoring the growth of turbulence and mixing near the front.

660 The overall influence of convergence/divergence on  $Ri_g$  is small (salinity stretching and vortex  
661 stretching, the fourth and fifth terms in (10)), because the their effects on vertical salinity gradients  
662 and vertical shear largely cancel each other in  $Ri_g$ . The influence of channel curvature on  $Ri_g$   
663 is generally negligible in the constriction region where curvature is mild (only considering the  
664 horizontal curvature effect here).

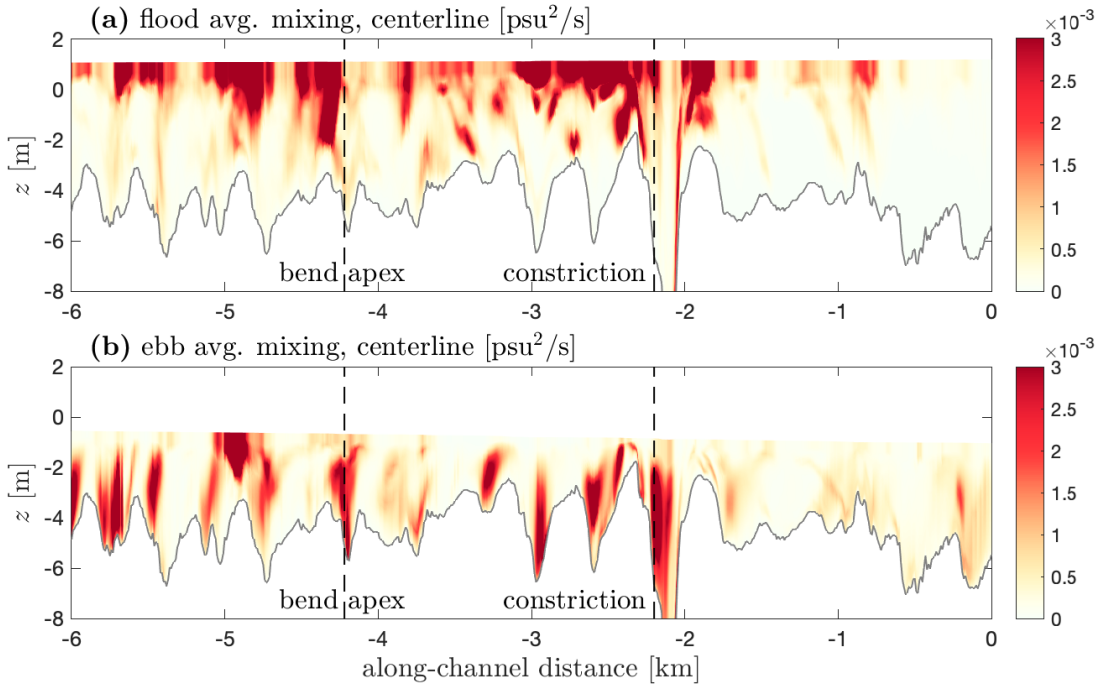
665 In addition to the mechanisms described above, other processes in the remainder term  $\mathcal{R}_{\mathcal{R}_T}$   
666 in (10), e.g., mixing, may also affect  $Ri_g$ . At the frontal zone, turbulent mixing of momentum  
667 (viscosity) tends to weaken the shear and increase  $Ri_g$ , while mixing of salinity tends to diffuse the  
668 salinity gradient and decrease  $Ri_g$ . Generally momentum mixing has a stronger influence on  $Ri_g$   
669 compared to salinity mixing because  $Ri_g$  depends on the square of shear, and their integrated effect  
670 is to increase  $Ri_g$  near the tidal intrusion front. The increasing tendency of  $Ri_g$  due to mixing is  
671 minimal at the surface convergence zone where  $Ri_g > 1$ , and it is not sufficient to counteract the  
672 overall decreasing tendency of  $Ri_g$  due to the integrated effects of baroclinicity, shear twisting, and  
673 salinity straining. However, the mixing effect is greater where  $Ri_g$  is close to the critical value  
674  $Ri_{g,cr}$ , leading to an increasing trend of  $Ri_g$  that counteracts other processes and can prevent  $Ri_g$   
675 from decreasing to less than  $Ri_{g,cr}$  (e.g., Trowbridge 1992; Geyer et al. 2017). Note that the overall

676 impact of mixing is not explicitly expressed in (10) because quantifying the influence of numerical  
677 mixing on  $Ri_g$  is challenging. We primarily refer to turbulent mixing in the discussion above, but  
678 in general numerical mixing is expected to act in a way similar to turbulent mixing.

679 In addition to the frontal zone, mixing also occurs over the shallow shoal in the southern part of  
680 XSC2 (Fig. 5 XSC2, at cross-channel distance of -50 m to 0 m). The influence of frontal dynamics  
681 and secondary circulation on  $Ri_g$ , in particular salinity straining and shear twisting, is weaker over  
682 the shoal compared to near the front. Instead, the bottom boundary layer has a greater influence on  
683  $Ri_g$  dynamics in this shallow region. As stratified water coming from the constriction encounters  
684 the shallow shoal, the strong bottom boundary shear and turbulence can decrease  $Ri_g$  and thus lead  
685 to mixing (i.e., mixing occurring inside the V-shape in the map view Fig. 12 (c)).

686 In the bend region, the processes that affect water column stability are mostly similar to the north-  
687 side front ( $F2_N$ ) in the constriction region. The straining of salinity tends to increase  $Ri_g$ , and the  
688 baroclinic exchange and vorticity twisting tend to decrease  $Ri_g$  at the sharp lateral front where the  
689 major counterclockwise secondary circulation cell occurs (Fig. 9). Moreover, the curvature effect  
690 also contributes to enhancing the shear, decreasing  $Ri_g$ , and destabilizing the water column in the  
691 bend, which is consistent with the more prominent contribution of CFA in the lateral momentum  
692 balance (see Eq. (3) and Fig. 10). Note that in the separation zone where the reversed (clockwise)  
693 secondary circulation cell occurs, the vorticity twisting term instead tends to twist vertical shear  
694 back into lateral shear and increase  $Ri_g$  locally (Fig. 9). In spite of the complexity of the smaller  
695 circulation cell within the separation zone, substantial mixing occurs near the frontal boundary  
696 where the counterclockwise secondary circulation occurs.

697 Overall, in both the constriction and bend regions, flow separation differentially advects salinity,  
698 interacts with secondary circulation, and leads to the generation of 3-d frontal structures. Intense  
699 mixing occurs at both the constriction and bend fronts, because the combined effects of baroclin-  
700 icity and twisting of shear by secondary circulation can enhance vertical shear and turbulence.  
701 Additionally, the curvature effect plays an important role in modulating convergence at the lateral  
702 salinity gradient through the bend.



704 FIG. 16. Vertical distribution of mixing along the North River centerline, from the mouth to 6 km into the  
 705 estuary. **(a)**: Flood tide average. **(b)**: Ebb tide average.

703 *f. The importance of near-surface mixing*

706 The mixing associated with flood tide intrusion fronts occurs primarily in the upper water column,  
 707 in contrast to bottom-generated turbulence and mixing that is usually dominant in shallow tidal  
 708 estuaries without winds (e.g., Stacey et al. 1999; Geyer et al. 2000; Scully et al. 2011). To illustrate  
 709 the tidal asymmetry in mixing, the time-averaged mixing along the North River centerline during  
 710 the flood and ebb tide is compared in Fig. 16. During the ebb tide, the strongest mixing generally  
 711 occurs in the lower water column in the bends, and that corresponds to bottom boundary layer  
 712 mixing at bend-scale bottom salinity fronts created by the channel curvature effect as proposed by  
 713 Bo and Ralston (2022). Note that an exception is found at around 5 km into the estuary where  
 714 mixing is mostly near the surface during the ebb tide. A tributary creek merges into the main stem  
 715 of the North River there (Garcia et al. 2021), and the plume of buoyant water from the creek leads  
 716 to near-surface mixing locally during the ebb tide.

717 In contrast to the ebb tide when most of the mixing is associated with the bottom boundary layer,  
 718 mixing during the flood tide occurs predominantly near the surface. We calculate the proportion

719 of mixing that happens in and outside of the bottom boundary layer to assess the contribution of  
720 near-surface mixing. The bottom boundary layer height  $H_{bbl}$  is defined based on the vertical shear  
721 stress (Reynolds stress) distribution in a similar way to Stacey and Ralston (2005), with  $H_{bbl}$  being  
722 the distance above the bed where shear stress becomes smaller than 10% of the bottom shear stress.  
723 Integrating along the estuary from the mouth to the ~ 7 km region with large bottom roughness  
724 (excluding the marsh platform and tributary channels), around 80% of mixing during the flood  
725 tide happens above the bottom boundary layer. This contrasts with the mixing during the ebb tide,  
726 where around half of the mixing occurs within the bottom boundary layer and most of the rest is  
727 near the top of the bottom boundary layer.

728 In addition to the flood-ebb asymmetry in the vertical distribution of mixing in the water column,  
729 we also calculate the temporal distribution of mixing between flood and ebb tides. During the  
730 spring tide with moderate discharge examined here, around 60% of the mixing occurs during the  
731 flood and 40% of the mixing occurs during the ebb tide. With mixing mostly occurring in the  
732 upper water column during the flood tide, the near-surface mixing associated with tidal intrusion  
733 fronts is thus of comparable importance to bottom boundary layer mixing in this system.

## 734 4. Discussion

### 735 a. Key mechanisms

736 We investigated the tidal intrusion fronts that occur during flood tides near two types of topo-  
737 graphic features, i.e., a constriction and a bend, as well as their influences on stratification and  
738 mixing. Downstream of the channel constriction, flow separation occurs on both sides of the jet  
739 flow from the narrow opening. The strong lateral shear zones between the jet and ambient flow  
740 create sharp lateral salinity gradients through differential advection. The resulting lateral baroclinic  
741 forcing leads to a pair of counter-rotating secondary circulation cells with convergence near the  
742 surface. Driven by secondary circulation, the fresher ambient water on both sides of the saltier jet  
743 propagates toward the center near the surface (surface-converging lateral gravity currents). The  
744 competition between lateral surface currents and the along-channel jet flow leads to the oblique  
745 angle of surface fronts to the streamwise direction that have a nearly critical Froude number in  
746 the front-normal direction. As the saltier jet flow encounters the frontal zone it subducts into the

747 lower layer of landward flow. Therefore, a tidal intrusion front is generated downstream of the  
748 constriction, with a classical V-shaped convergence zone near the surface.

749 Stratification is created at the tidal intrusion front as a result of lateral straining by the BCPG-  
750 driven secondary circulation. While stratification is expected to inhibit turbulence and mixing,  
751 intense turbulent mixing is found near the front. Mixing occurs because both the vertical shear of  
752 secondary circulation and the reversed vertical shear of streamwise velocity contribute to decreasing  
753  $Ri_g$  and destabilizing the water column. The reversed vertical shear of streamwise velocity, with  
754 the flood-tide current decreasing toward the water surface, results from the twisting of laterally  
755 sheared jet flow by the secondary circulation.

756 Analysis in the constriction region reveals that tidal intrusion fronts are hot spots of mixing,  
757 and similarly, channel bends can also lead to surface convergence fronts with intensified mixing.  
758 In the bend, flow separation occurs near the inner bank behind the bend apex as a result of the  
759 channel curvature effect. Similar to the constriction region, lateral salinity gradients are enhanced  
760 at the boundary of the separation zone as a result of differential advection and lead to secondary  
761 circulation through BCPG forcing. A tidal intrusion front occurs with the surface convergence zone  
762 being oblique to the main flow, spanning from the bend apex on the inner bank to the downstream  
763 outer bank. Enhanced mixing occurs at the tidal intrusion front in the upper water column, akin to  
764 the constriction region. In contrast to the V-shaped front downstream of the constriction, the tidal  
765 intrusion front in the bend resembles half of a V-shape and can be regarded as a one-sided tidal  
766 intrusion front, since flow separation only occurs on the inner bank. Moreover, while the lateral  
767 BCPG dominates in the constriction region, the additional CFA due to the channel curvature effect  
768 has a comparable magnitude to BCPG in the bend. The combined influences of curvature and  
769 baroclinicity result in more complex secondary circulation, frontogenesis, vertical shear generation,  
770 and mixing.

771 Based on a salinity variance budget analysis, the mixing associated with tidal intrusion fronts is  
772 capable of destroying the stratification created by lateral straining. Furthermore, this mixing occurs  
773 predominantly near the surface during the flood tide, in contrast to the ebb tide when mixing mostly  
774 occurs in the lower water column. The flood tide near-surface mixing is found to be comparable to  
775 the bottom boundary layer mixing during the ebb tide in the North River estuary.

776 *b. Instability and mixing*

777 White and Helfrich (2013) conducted an idealized numerical study of a horizontal shear layer with  
778 a horizontal density gradient, and described two end-member regimes where instabilities can grow,  
779 i.e., a pure well-mixed horizontal shear layer and a pure gravity current without horizontal shear.  
780 Our analysis provides a realistic intermediate case between the two end-member regimes, where  
781 the interaction between lateral shear and lateral gravity current can generate a third component of  
782 vorticity, i.e., the reversed vertical shear of streamwise velocity near the surface, and this reversed  
783 shear is also important for destabilizing the water column and leading to turbulent mixing. The  
784 vorticity twisting and near-surface turbulence and mixing is also consistent with observations in  
785 Collignon and Stacey (2013) and Huguenard et al. (2015).

786 By contrast, Giddings et al. (2012) reported inhibition of turbulence near a lateral front in late  
787 flood tide. That could be a case where the additional reversed shear resulting from vorticity twisting  
788 was less influential because the streamwise tidal current was weak during the late flood stage. In  
789 those observations, the vertical shear of lateral gravity current alone was insufficient to overcome  
790 the stabilizing effect of stratification from straining.

791 Simpson and Linden (1989) found that for 2-d gravity currents with a uniform horizontal density  
792 gradient, baroclinicity can only asymptotically decrease  $Ri_g$  to 0.5. To further decrease  $Ri_g$  and lead  
793 to the growth of instability, either non-uniformity in the horizontal density gradient (Simpson and  
794 Linden 1989) or velocity convergence due to topographic forcing (Geyer and Ralston 2015; Geyer  
795 et al. 2017) is needed (corresponding to the fourth and fifth terms in Eq. (10)). As a comparison  
796 to the classical 2-d scenario, the present study highlights the importance of 3-d processes for  
797 decreasing  $Ri_g$  and leading to frontal instability and mixing, in particular the interaction between  
798 cross-front gravity currents (baroclinic secondary circulation) and along-front background currents  
799 that was not represented in Simpson and Linden (1989).

800 This research suggests that the influence of flow curvature on water column instability and  
801 mixing is small in the constriction region. However, the channel curvature effect can be an  
802 important contributor to secondary circulation, enhanced vertical shear, and turbulence in channel  
803 bends, and thus provides an additional source of mixing in sinuous estuaries.

804    *c. Broader implications*

805    The analysis presented here focused on a spring tide with moderate discharge conditions and  
806    found that around 60% of the mixing occurs during the flood tide, primarily associated with surface  
807    fronts. In model results, the intensified mixing at surface fronts during flood tides consistently  
808    occurs across spring-neap cycles and under varying river forcing conditions. The fraction of  
809    the total mixing during flood tides varies between 30% and 60% during the simulation period,  
810    with the minimum flood-to-ebb ratio during neap tides with high river discharge in late October  
811    2021. During that period, flood tide mixing still mostly happens near the surface and is associated  
812    with tidal intrusion fronts. Tidal currents (and thus the lateral shear) are weaker during neap tides,  
813    which leads to weaker differential advection and smaller lateral salinity gradients to drive secondary  
814    circulation and surface convergence. As corroborating evidence, the surface convergence features  
815    are generally less noticeable in both the model and observations during neap tides than spring tides.  
816    In addition, stronger stratification appears during that period due to the weaker tidal currents and  
817    higher river flow, and stratification can suppress secondary circulation (Chant and Wilson 1997)  
818    and thus hinder the development of fronts and mixing. By contrast, intense mixing still occurs  
819    during the ebb stage when the pycnocline meets regions with strong bottom boundary turbulence,  
820    even with the stronger stratification. While the flood tide accounts for a smaller portion of the  
821    mixing during neap tides and high discharge, surface fronts remain an important factor in the total  
822    mixing and stratification in the estuary.

823    Similar near-surface mixing is also expected to occur in other estuaries where tidal intrusion  
824    fronts have been observed (e.g., Simpson and Nunes 1981; Largier 1992; Marmorino and Trump  
825    1996). In particular, strong tidal currents and topographic features that can enhance the lateral  
826    shear are important for differential advection, frontogenesis, and mixing. Additionally, moderate  
827    stratification could favor the formation of fronts, as strong stratification may inhibit secondary  
828    circulation and thus the occurrence of convergence. With weak stratification, secondary circulation  
829    is still likely to occur, but it might lead to axial convergence fronts instead of classical tidal intrusion  
830    fronts (Nunes and Simpson 1985; Simpson and Turrell 1986).

831    Nunes and Simpson (1985) studied axial convergence fronts, and used an analytical solution to  
832    predict the strength of the associated secondary flow with the magnitude of lateral salinity gradient.  
833    We examined their analytical prediction with the tidal intrusion fronts and secondary circulation

in our model. At the constriction, the analytical solution is generally effective in predicting the strength of secondary circulation based on the lateral salinity gradient due to differential advection. While the Nunes and Simpson (1985) solution assumed that the lateral pressure gradient forcing is balanced by friction, the frictional effect is relatively weak our results (Figs. 6), and the advection term replaces friction in balancing the pressure gradient forcing (Nidzieko et al. 2009; Kranenburg et al. 2019). In the bend region, the secondary circulation from the analytical prediction by Nunes and Simpson (1985) is correlated with the model results but has a much smaller magnitude. This discrepancy is likely due to the influence of the centrifugal forcing of flow curvature on the secondary circulation in addition to baroclinic forcing from differential advection.

Nevertheless, the correlation between the Nunes and Simpson (1985) solution and our model results indicates the intrinsic similarities between axial convergence fronts and tidal intrusion fronts, in terms of the lateral shear, differential advection, BCPG-driven secondary circulation, and surface convergence. We further speculate that the axial convergence front corresponds to an instance of the tidal intrusion front with weak stratification, even though they are named differently. The lateral gravity current propagation speed is small compared to the streamwise velocity when horizontal and vertical salinity gradients are weak, and the surface front thus resembles a single convergence line following the channel orientation, instead of exhibiting a conspicuous oblique angle to the upstream flow.

In addition, plume fronts were suggested to be dynamically related to tidal intrusion fronts as both have buoyancy-driven flow structures (O'Donnell 1993). Tidal intrusion fronts typically occur as saltier water is forced into estuaries by the strong flood tide current. The flood current may therefore oppose the motion of buoyant ambient water inside estuaries (moving at internal disturbance propagation speed), leading to a strong surface convergence zone with an oblique angle to the flood current. By comparison, in a river plume where fresher water discharges into saltier water, the internal disturbance propagation direction usually conforms to the direction of the inertial momentum of plume water. Therefore, the shape of a plume may be more dispersed on the surface compared to the V-shape found in tidal intrusion fronts (Armi and Farmer 1986; Largier 1992). Nevertheless, the existence of ambient coastal current can introduce in additional momentum that is against the plume, which may thus sharpen the shape of plume and lead to intense surface convergence and mixing (O'Donnell 1997; MacDonald and Geyer 2005).

864 **5. Conclusion**

865 We studied tidal intrusion fronts during flood tides in an estuary with complex topography, with  
866 a particular focus on two topographic features, i.e., channel constrictions and bends. Flow separa-  
867 tion and differential advection are important for creating lateral salinity gradients at both locations,  
868 which drives secondary circulation through baroclinicity and generates surface convergence fronts,  
869 or tidal intrusion fronts. Secondary circulation creates stratification at fronts through lateral strain-  
870 ing, and also enhances vertical shear through baroclinic exchange and twisting of the streamwise  
871 shear to lead to intense mixing near fronts. The constriction and bend regions have different frontal  
872 shapes as a result of differences in flow separation due to channel geometry. Moreover, channel  
873 curvature in bends also affects secondary circulation, frontogenesis, vertical shear, and mixing,  
874 along with baroclinicity. Overall, the near-surface mixing that is primarily associated with tidal  
875 intrusion fronts is similar in magnitude to bottom boundary layer mixing in this estuary.

876 *Acknowledgments.* The research leading to these results was funded by NSF awards OCE-  
877 2123002 and OCE-1634481. The authors thank Peter Traykovski for providing the bathymetric  
878 data and Jay Sisson, Sean Whelan, Salme Cook, and Noa Randall for fieldwork assistance.

879 *Data availability statement.* Model data supporting this study are available online  
880 at <https://doi.org/10.5281/zenodo.8126968>; observational data are available online at  
881 <https://doi.org/10.5281/zenodo.10059736>.

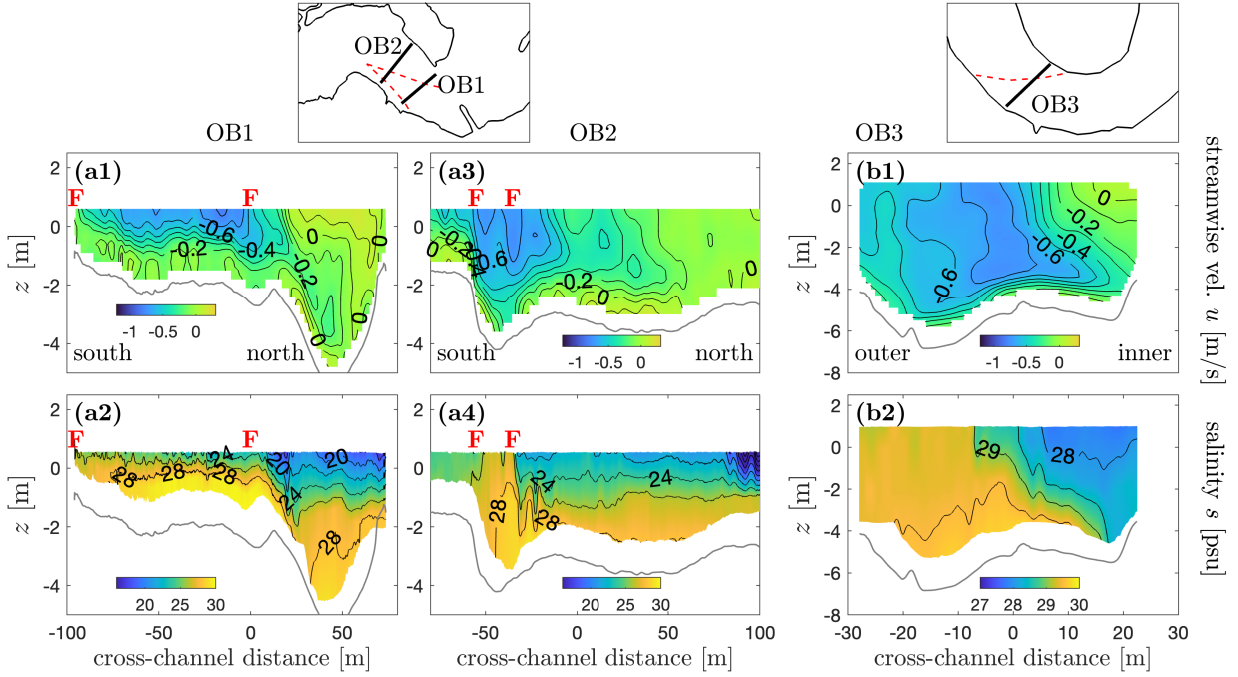
882 **APPENDIX**

883 **APPENDIX A**

884 **Shipboard surveys at the constriction and bend**

885 During the observational period, shipboard surveys were conducted at multiple cross-sections  
886 and along-channel sections near the constriction and in several bends in the North River estuary.  
887 Continuous salinity and temperature data were collected with a towed CTD array that had three or  
888 four CTD sensors in the vertical, and velocity profile data were collected with a shipboard acoustic  
889 Doppler current profiler. The sensor depths of the towed array were actively adjusted depending on  
890 the local bathymetry to maximize the vertical coverage, with a typical vertical spacing of 0.5 – 2 m  
891 between sensors. The towed array sampling was needed to resolve sharp density gradients at fronts  
892 better than possible with discrete CTD profiles.

893 Measurements in several representative cross-sections are presented that correspond with regions  
894 and tidal stages with the occurrence of surface convergence fronts (Fig. A1). Landward of the  
895 constriction, faster velocity occurs on the southern part of the cross-sections during the flood tide,  
896 which corresponds with the strong jet flow from the narrow opening (OB1 and OB2 in Fig. A1). The  
897 faster velocity brings higher salinity water landward by differential advection and creates lateral  
898 salinity gradients across the lateral shear zones. The lateral salinity gradients can thus create  
899 secondary circulation and lead to the V-shaped surface convergence front (see the drone imagery  
900 in Fig. 3 (a)), and the detailed mechanisms are explained in the numerical analysis (section 3 c).  
901 Note that the V-shape can also be inferred by comparing the width of the high-velocity and high-  
902 salinity region in OB1 and OB2. The velocity and salinity fields in the model (Fig. 5) are generally  
903 consistent with these observational results.



893 FIG. A1. Shipboard measurements of streamwise velocity and salinity during spring flood tides. **(a1)-(a4):**  
 894 Two cross-sections landward of the constriction at around 2 km into the estuary (at 10 am on Oct 7, 2021).  
 895 Negative velocity is landward (flood direction). The red “F”s mark the V-shaped surface convergence front.  
 896 **(b1)-(b2):** A cross-section in the bend at around 5.5 km into the estuary (at 11 am on Nov 5, 2021). Locations of  
 897 cross-sections are shown on the small maps, with red lines delineating the surface fronts. Note that the shipboard  
 898 measurements and drone surveys in Fig. 3 are conducted at different times but similar tidal conditions and stages.

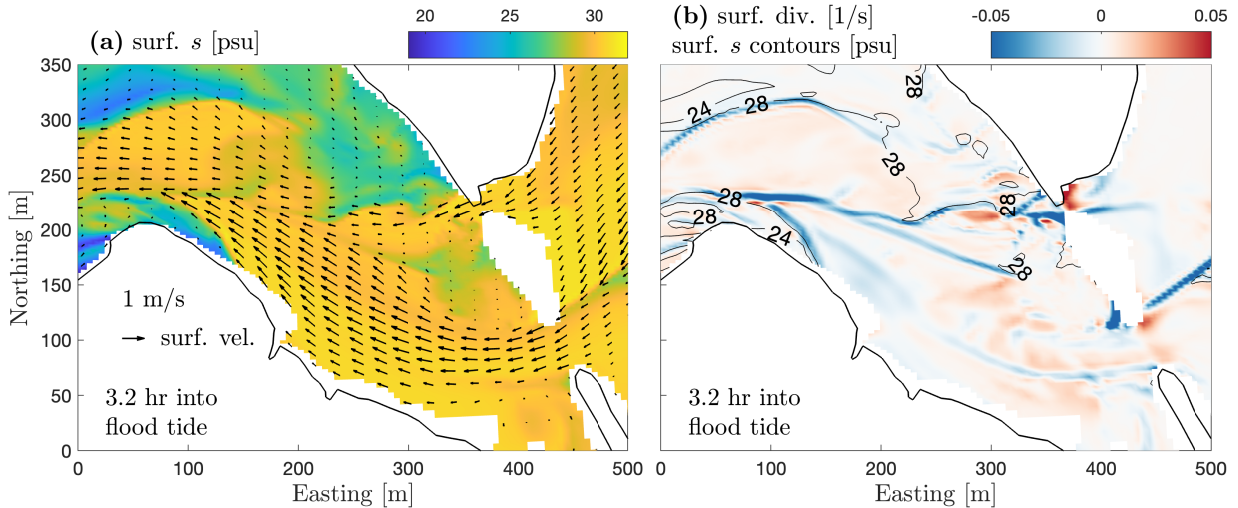
910 In the bend at around 5.5 km into the estuary, flow separation occurs during the flood tide at the  
 911 bend apex and creates the low-velocity zone near the inner bank (OB3 in Fig. A1). The laterally  
 912 sheared flow differentially advects salinity and thus leads to low salinity in the inner bank. The  
 913 lateral salinity gradient contributes to the development of secondary circulation that can further  
 914 interact with the main flow and generate the oblique surface convergence front (see the drone  
 915 imagery in Fig. 3 **(b)**; mechanisms examined in the model analysis in section 3 c).

916

## APPENDIX B

917

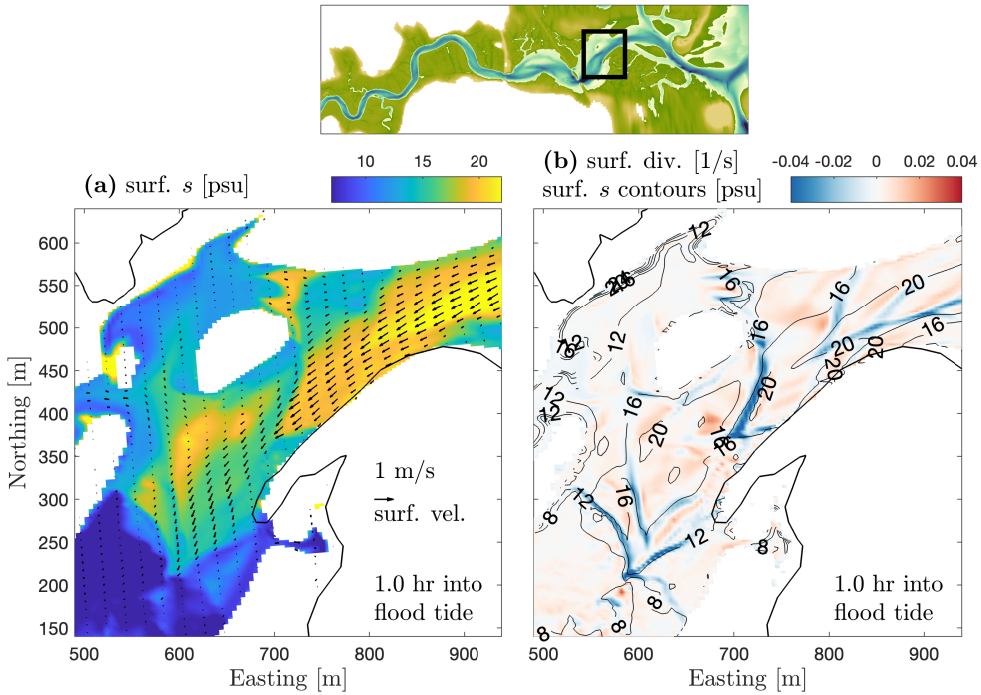
### Modeled surface fronts at multiple locations



918 FIG. B1. The constriction region. **(a)**: Surface salinity. Arrows show surface velocity. **(b)**: Divergence of  
 919 surface velocity, with blue colors representing surface convergence. This is the same region as Fig. 4, but at a  
 920 later stage into the flood tide.

927 The snapshot shown in Fig. B1 is around one hour later than that in Fig. 4. The V-shaped front  
 928 shifts slightly landward by  $\sim 50 - 100$  m and has a less oblique angle with respect to the main flow  
 929 in this later snapshot. These shifts are primarily due to the weaker stratification later in the flood  
 930 tide, which leads to an increased composite Froude number  $G$ . As a result, a more acute angle is  
 931 required to satisfy the critical condition  $G \sin \phi \approx 1$  at the front. The later snapshot is closer to the  
 932 tidal stage when the drone imagery was captured, and the V-shaped front is more similar to the one  
 933 shown in the drone imagery. Refer to the Supplemental Material for a movie of the model results  
 934 in this region through a flood tide.

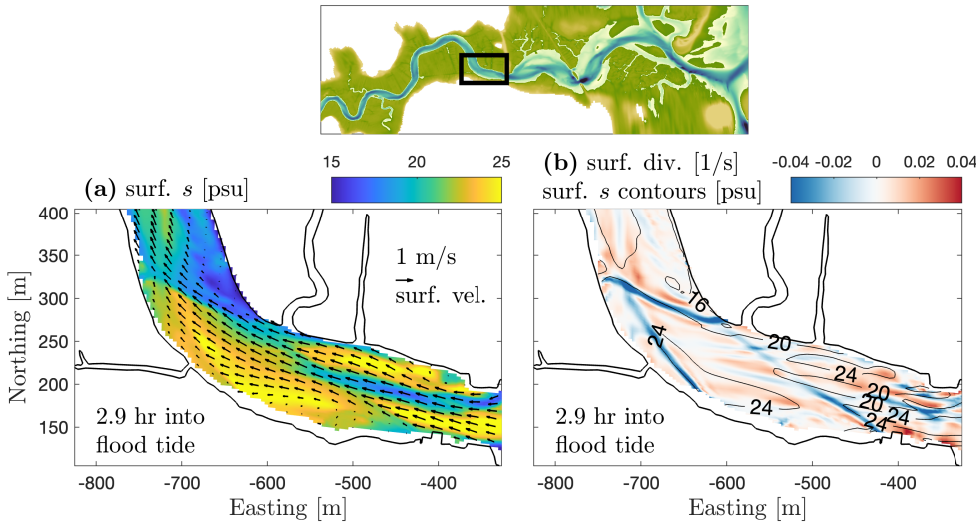
935 In addition to the constriction and bend regions discussed in the main text, surface convergence  
 936 fronts also occur in other areas in the North River estuary. In a region between the estuary mouth  
 937 and the constriction, multiple V-shaped surface fronts emerge due to abrupt changes in channel  
 938 width associated with shoal regions (see Fig. B2). These fronts exhibit similar frontal dynamics  
 939 and intense mixing, akin to the one near the constriction. In another region between the constriction  
 940 and bend1, a surface convergence front forms as the flood current changes direction in the channel  
 941 (Fig.B3). Note that this region includes a bridge located in the bottom right part of Fig.B3 at  
 942 around  $-400$  m Easting, and the complex bathymetry attributed to anthropogenic influences may  
 943 add to the variability in the salinity field.



921 FIG. B2. A region between the estuary mouth and the constriction, at around 1.8 km from the mouth,  
 922 corresponding to the rectangle in the bathymetric map. (a): Surface salinity. Arrows show surface velocity. (b):  
 923 Divergence of surface velocity, with blue colors representing surface convergence.

## 944 References

- 945 Armi, L., and D. Farmer, 1986: Maximal two-layer exchange through a contraction with barotropic  
 946 net flow. *Journal of Fluid Mechanics*, **164**, 27–51.
- 947 Becherer, J., M. T. Stacey, L. Umlauf, and H. Burchard, 2015: Lateral circulation generates  
 948 flood tide stratification and estuarine exchange flow in a curved tidal inlet. *Journal of Physical  
 949 Oceanography*, **45** (3), 638–656.
- 950 Blanckaert, K., 2015: Flow separation at convex banks in open channels. *Journal of Fluid Me-  
 951 chanics*, **779**, 432–467.
- 952 Bo, T., and D. K. Ralston, 2020: Flow separation and increased drag coefficient in estuarine  
 953 channels with curvature. *Journal of Geophysical Research: Oceans*, **125** (10), e2020JC016 267.
- 954 Bo, T., and D. K. Ralston, 2022: Frontogenesis, mixing, and stratification in estuarine channels  
 955 with curvature. *Journal of Physical Oceanography*.



924 FIG. B3. A region between the constriction and bend1, at around 3 km from the estuary mouth, corresponding  
 925 to the rectangle in the bathymetric map. (a): Surface salinity. Arrows show surface velocity. (b): Divergence of  
 926 surface velocity, with blue colors representing surface convergence.

956 Bo, T., D. K. Ralston, and W. R. Geyer, 2023: Sources of drag in estuarine meanders: momen-  
 957 tum redistribution, bottom stress enhancement, and bend-scale form drag. *Journal of Physical*  
 958 *Oceanography*.

959 Bo, T., D. K. Ralston, W. M. Kranenburg, W. R. Geyer, and P. Traykovski, 2021: High and variable  
 960 drag in a sinuous estuary with intermittent stratification. *Journal of Geophysical Research: Oceans*, **126** (10), e2021JC017327.

962 Brown, J., W. Turrell, and J. Simpson, 1991: Aerial surveys of axial convergent fronts in uk  
 963 estuaries and the implications for pollution. *Marine Pollution Bulletin*, **22** (8), 397–400.

964 Burchard, H., and H. Rennau, 2008: Comparative quantification of physically and numerically  
 965 induced mixing in ocean models. *Ocean Modelling*, **20** (3), 293–311.

966 Chant, R. J., and R. E. Wilson, 1997: Secondary circulation in a highly stratified estuary. *Journal*  
 967 *of Geophysical Research: Oceans*, **102** (C10), 23 207–23 215.

968 Collignon, A. G., and M. T. Stacey, 2012: Intratidal dynamics of fronts and lateral circulation at  
 969 the shoal–channel interface in a partially stratified estuary. *Journal of physical oceanography*,  
 970 **42** (5), 869–883.

- 971 Collignon, A. G., and M. T. Stacey, 2013: Turbulence dynamics at the shoal–channel interface in  
972 a partially stratified estuary. *Journal of physical oceanography*, **43** (5), 970–989.
- 973 Dietrich, W. E., and J. D. Smith, 1983: Influence of the point bar on flow through curved channels.  
974 *Water Resources Research*, **19** (5), 1173–1192.
- 975 Garcia, A. M. P., W. R. Geyer, and N. Randall, 2021: Exchange flows in tributary creeks enhance  
976 dispersion by tidal trapping. *Estuaries and Coasts*, 1–19.
- 977 Garvine, R. W., 1974: Dynamics of small-scale oceanic fronts. *Journal of Physical Oceanography*,  
978 **4** (4), 557–569.
- 979 Geyer, W. R., 1993: Three-dimensional tidal flow around headlands. *Journal of Geophysical  
980 Research: Oceans*, **98** (C1), 955–966.
- 981 Geyer, W. R., and D. K. Ralston, 2015: Estuarine frontogenesis. *Journal of Physical Oceanography*,  
982 **45** (2), 546–561.
- 983 Geyer, W. R., D. K. Ralston, and J.-L. Chen, 2020: Mechanisms of exchange flow in an estuary with  
984 a narrow, deep channel and wide, shallow shoals. *Journal of Geophysical Research: Oceans*,  
985 **125** (12), e2020JC016092.
- 986 Geyer, W. R., D. K. Ralston, and R. C. Holleman, 2017: Hydraulics and mixing in a laterally  
987 divergent channel of a highly stratified estuary. *Journal of Geophysical Research: Oceans*,  
988 **122** (6), 4743–4760.
- 989 Geyer, W. R., J. H. Trowbridge, and M. M. Bowen, 2000: The dynamics of a partially mixed  
990 estuary. *Journal of Physical Oceanography*, **30** (8), 2035–2048.
- 991 Giddings, S. N., and Coauthors, 2012: Frontogenesis and frontal progression of a trapping-  
992 generated estuarine convergence front and its influence on mixing and stratification. *Estuaries  
993 and Coasts*, **35** (2), 665–681.
- 994 Haidvogel, D. B., and Coauthors, 2008: Ocean forecasting in terrain-following coordinates: For-  
995 mulation and skill assessment of the regional ocean modeling system. *Journal of Computational  
996 Physics*, **227** (7), 3595–3624.

- Howard, L. N., 1961: Note on a paper of john w. miles. *Journal of Fluid Mechanics*, **10** (4), 509–512.
- Huguenard, K., A. Valle-Levinson, M. Li, R. Chant, and A. Souza, 2015: Linkage between lateral circulation and near-surface vertical mixing in a coastal plain estuary. *Journal of Geophysical Research: Oceans*, **120** (6), 4048–4067.
- Kalkwijk, J. P. T., and R. Booij, 1986: Adaptation of secondary flow in nearly-horizontal flow. *Journal of Hydraulic Research*, **24** (1), 19–37.
- Kalra, T. S., X. Li, J. C. Warner, W. R. Geyer, and H. Wu, 2019: Comparison of physical to numerical mixing with different tracer advection schemes in estuarine environments. *Journal of Marine Science and Engineering*, **7** (10), 338.
- Kranenburg, W. M., W. R. Geyer, A. M. P. Garcia, and D. K. Ralston, 2019: Reversed lateral circulation in a sharp estuarine bend with weak stratification. *Journal of Physical Oceanography*.
- Lacy, J. R., and S. G. Monismith, 2001: Secondary currents in a curved, stratified, estuarine channel. *Journal of Geophysical Research: Oceans*, **106** (C12), 31 283–31 302.
- Lacy, J. R., M. T. Stacey, J. R. Burau, and S. G. Monismith, 2003: Interaction of lateral baroclinic forcing and turbulence in an estuary. *Journal of Geophysical Research: Oceans*, **108** (C3).
- Largier, J. L., 1992: Tidal intrusion fronts. *Estuaries*, **15** (1), 26–39.
- Largier, J. L., 1993: Estuarine fronts: how important are they? *Estuaries*, **16** (1), 1–11.
- Leeder, M. R., and P. H. Bridges, 1975: Flow separation in meander bends. *Nature*, **253**, 1–2.
- Leopold, L. B., and M. G. Wolman, 1960: River meanders. *Geological Society of America Bulletin*, **71** (6), 769–793.
- Lerczak, J. A., and W. R. Geyer, 2004: Modeling the lateral circulation in straight, stratified estuaries. *Journal of Physical Oceanography*, **34** (6), 1410–1428.
- Li, M., P. Cheng, R. Chant, A. Valle-Levinson, and K. Arnott, 2014: Analysis of vortex dynamics of lateral circulation in a straight tidal estuary. *Journal of Physical Oceanography*, **44** (10), 2779–2795.

- 1023 Li, X., W. R. Geyer, J. Zhu, and H. Wu, 2018: The transformation of salinity variance: A new  
1024 approach to quantifying the influence of straining and mixing on estuarine stratification. *Journal*  
1025 *of Physical Oceanography*, **48** (3), 607–623.
- 1026 Luettich, R. A., J. J. Westerink, N. W. Scheffner, and Coauthors, 1992: ADCIRC: an advanced  
1027 three-dimensional circulation model for shelves, coasts, and estuaries. report 1, theory and  
1028 methodology of ADCIRC-2DD1 and ADCIRC-3DL. Tech. rep., Dredging Research Program  
1029 Technical Report DRP-92-6, U.S. Army Engineers Waterways Experiment Station.
- 1030 MacDonald, D. G., and W. R. Geyer, 2005: Hydraulic control of a highly stratified estuarine front.  
1031 *Journal of physical oceanography*, **35** (3), 374–387.
- 1032 Marani, M., S. Lanzoni, D. Zandolin, G. Seminara, and A. Rinaldo, 2002: Tidal meanders. *Water*  
1033 *Resources Research*, **38** (11), 7–1–7–14.
- 1034 Marmorino, G., and C. Trump, 1996: High-resolution measurements made across a tidal intrusion  
1035 front. *Journal of Geophysical Research: Oceans*, **101** (C11), 25 661–25 674.
- 1036 McWilliams, J. C., 2021: Oceanic frontogenesis. *Annual Review of Marine Science*, **13**, 227–253.
- 1037 Miles, J. W., 1961: On the stability of heterogeneous shear flows. *Journal of Fluid Mechanics*,  
1038 **10** (4), 496–508.
- 1039 Murphy, A. H., 1988: Skill scores based on the mean square error and their relationships to the  
1040 correlation coefficient. *Monthly weather review*, **116** (12), 2417–2424.
- 1041 Nidzieko, N. J., J. L. Hench, and S. G. Monismith, 2009: Lateral Circulation in Well-Mixed and  
1042 Stratified Estuarine Flows with Curvature. *Journal of Physical Oceanography*, **39** (4), 831–851.
- 1043 Nunes, R., and J. Simpson, 1985: Axial convergence in a well-mixed estuary. *Estuarine, Coastal*  
1044 *and Shelf Science*, **20** (5), 637–649.
- 1045 O'Donnell, J., 1993: Surface fronts in estuaries: a review. *Estuaries*, **16** (1), 12–39.
- 1046 O'Donnell, J., 1997: Observations of near-surface currents and hydrography in the connecticut  
1047 river plume with the surface current and density array. *Journal of Geophysical Research: Oceans*,  
1048 **102** (C11), 25 021–25 033.

- 1049 Ralston, D. K., G. W. Cowles, W. R. Geyer, and R. C. Holleman, 2017: Turbulent and numerical  
1050 mixing in a salt wedge estuary: Dependence on grid resolution, bottom roughness, and turbulence  
1051 closure. *Journal of Geophysical Research: Oceans*, **122** (1), 692–712.
- 1052 Ralston, D. K., and M. T. Stacey, 2005: Longitudinal dispersion and lateral circulation in the  
1053 intertidal zone. *Journal of Geophysical Research: Oceans*, **110** (C7).
- 1054 Scully, M. E., and W. R. Geyer, 2012: The role of advection, straining, and mixing on the tidal  
1055 variability of estuarine stratification. *Journal of Physical Oceanography*, **42** (5), 855–868.
- 1056 Scully, M. E., W. R. Geyer, and J. H. Trowbridge, 2011: The influence of stratification and nonlocal  
1057 turbulent production on estuarine turbulence: An assessment of turbulence closure with field  
1058 observations. *Journal of Physical Oceanography*, **41** (1), 166–185.
- 1059 Shchepetkin, A. F., and J. C. McWilliams, 2005: The regional oceanic modeling system (roms): a  
1060 split-explicit, free-surface, topography-following-coordinate oceanic model. *Ocean modelling*,  
1061 **9** (4), 347–404.
- 1062 Simpson, J., and P. Linden, 1989: Frontogenesis in a fluid with horizontal density gradients.  
1063 *Journal of Fluid Mechanics*, **202**, 1–16.
- 1064 Simpson, J., and R. Nunes, 1981: The tidal intrusion front: an estuarine convergence zone.  
1065 *Estuarine Coastal and Shelf Science*, **13** (3), 257–IN1.
- 1066 Simpson, J., and W. Turrell, 1986: Convergent fronts in the circulation of tidal estuaries. *Estuarine  
1067 variability*, Elsevier, 139–152.
- 1068 Stacey, M. T., S. G. Monismith, and J. R. Burau, 1999: Observations of turbulence in a partially  
1069 stratified estuary. *Journal of Physical Oceanography*, **29** (8), 1950–1970.
- 1070 Stacey, M. T., and D. K. Ralston, 2005: The scaling and structure of the estuarine bottom boundary  
1071 layer. *Journal of Physical Oceanography*, **35** (1), 55–71.
- 1072 Thomson, J., 1877: V. on the origin of windings of rivers in alluvial plains, with remarks on the  
1073 flow of water round bends in pipes. *Proceedings of the Royal Society of London*, **25** (171-178),  
1074 5–8.

- 1075 Trowbridge, J., 1992: A simple description of the deepening and structure of a stably stratified flow  
1076 driven by a surface stress. *Journal of Geophysical Research: Oceans*, **97** (C10), 15 529–15 543.
- 1077 Tyler, M. A., D. W. Coats, and D. M. Anderson, 1982: Encystment in a dynamic environment:  
1078 deposition of dinoflagellate cysts by a frontal convergence. *Marine Ecology Progress Series*,  
1079 163–178.
- 1080 Umlauf, L., and H. Burchard, 2003: A generic length-scale equation for geophysical turbulence  
1081 models. *Journal of Marine Research*, **61** (2), 235–265.
- 1082 Valle-Levinson, A., C. Li, K.-C. Wong, and K. M. Lwiza, 2000: Convergence of lateral flow along  
1083 a coastal plain estuary. *Journal of Geophysical Research: Oceans*, **105** (C7), 17 045–17 061.
- 1084 Wang, T., and Coauthors, 2022: Accumulation, transformation and transport of microplastics in  
1085 estuarine fronts. *Nature Reviews Earth & Environment*, **3** (11), 795–805.
- 1086 Warner, J. C., B. Armstrong, R. He, and J. B. Zambon, 2010: Development of a coupled ocean–  
1087 atmosphere–wave–sediment transport (coawst) modeling system. *Ocean modelling*, **35** (3), 230–  
1088 244.
- 1089 Warner, J. C., Z. Defne, K. Haas, and H. G. Arango, 2013: A wetting and drying scheme for  
1090 ROMS. *Computers & geosciences*, **58**, 54–61.
- 1091 Warner, J. C., C. R. Sherwood, H. G. Arango, and R. P. Signell, 2005: Performance of four  
1092 turbulence closure models implemented using a generic length scale method. *Ocean Modelling*,  
1093 **8** (1-2), 81–113.
- 1094 Warner, J. C., C. R. Sherwood, R. P. Signell, C. K. Harris, and H. G. Arango, 2008: Development of  
1095 a three-dimensional, regional, coupled wave, current, and sediment-transport model. *Computers  
1096 & geosciences*, **34** (10), 1284–1306.
- 1097 White, B. L., and K. R. Helfrich, 2013: Rapid gravitational adjustment of horizontal shear flows.  
1098 *Journal of Fluid Mechanics*, **721**, 86–117.